LRP 462/92 August 1992

Invited and Contributed Papers
presented at the

Joint Varenna-Lausanne International Workshop on "Theory of Fusion Plasmas" Varenna, Italy, August 24-28, 1992

by the
Theory Group

LIST OF CONTENTS

IDEAL AND RESISTIVE MHD STABILITY OF INTERNAL KINK MODES IN CIRCULAR AND SHAPED TOKAMAKS

A. Bondeson[a], G. Vlad[b] and H. Lütjens[a]

[a]Centre de Recherches en Physique des Plasmas, Association Euratom - Confédération Suisse, Ecole Polytechnique Fédérale de Lausanne, Lausanne, Switzerland

[b]Associazione Euratom - ENEA sulla Fusione, C.R.E. Frascati, Rome, Italy

Abstract: Recent results for the MHD stability of internal kink modes in tokamaks are reviewed. In general, ideal stability is more restrictive than the conventionally cited limit $\beta_p < 0.3$ (where β_p is the poloidal beta at the $q = 1$ surface). This holds, in particular, for shaped equilibria, where low shear in combination with elliptic shaping can drastically reduce the pressure limit. Also in resistive MHD, interchange effects are frequently destabilizing, and resistive stability at $\beta_p \geq 0.05$ is achieved, for circular cross section, only with a very restricted class of current profiles, and not at all for JET-shaped cross section.

1. INTRODUCTION

Since their discovery in the ST tokamak by von Goeler, et al [1], the sawtooth oscillations have been the subject of many experimental and theoretical studies, see, e.g., [2 - 15]. Experimental observations in large tokamaks have revealed a large variety of behaviors, and although theory has made progress, many experimental observations remain unexplained. Undoubtedly, several of these require more sophisticated theories than magnetohydrodynamics (MHD) for their explanation. However, it is also clear that a

2

significant source of the varied behavior, and the theoretical difficulties, lies in the fact that the triggering instability - the internal kink mode - is weak. It is sensitive to a large number of effects, some of which *are* included in the MHD description. The purpose of this talk is to discuss in some detail the MHD stability of the internal kink. The main conclusion is that the often quoted stability limit (in terms of poloidal beta at the q = 1 surface); $\beta_{p,crit} \approx 0.3$, is generally overly optimistic and that the internal kink is considerably more unstable than previously assumed, in particular in tokamaks of elliptic cross section.

The results shown here are drawn mainly from two recent papers [16, 17], where internal kinks are studied for a variety of profiles and with different plasma cross sections. The numerical calculations have been made using the cubic element equilibrium code CHEASE [18] and the toroidal resistive stability code MARS [19]. These two codes allow more or less routine calculation of resistive instabilities at high Lundquist numbers (at least those characteristic of JET, $S \approx 10^9$) and with small growth rates, γ/ω_A down to 10^{-5}.

2. IDEAL STABILITY FOR CIRCULAR CROSS SECTION

In a pioneering paper, Bussac et al [7] developed a large aspect ratio expansion and calculated the pressure limit for internal kink stability in circular equilibria. For a parabolic current profile and a small q = 1 radius, they found that the mode is stable when $\beta_p < (13/144)^{1/2} \approx 0.3$. In carrying out numerical calculations at finite aspect ratio, we generally found significantly lower pressure limits [17]; examples are given in Figs. 1 and 2. The equilibria have circular boundary with aspect ratio $R_0/a = 4$, and the current profiles are specified by giving the flux surface averaged toroidal current density I* as a function of the normalized poloidal flux $\Psi = (\psi - \psi_0)/(\psi_a - \psi_0)$. (where ψ is the poloidal flux function and subscripts '0' and 'a' denote the magnetic axis and the plasma edge, respectively). $I^*(\Psi)$ is specified up to a normalization constant, which is adjusted to specify the q = 1 radius. The stability diagrams in Fig. 1 and 2 give β_p as a function of the normalized q = 1 radius ρ (proportional to the square-root of the enclosed volume) at constant growth rates, $\gamma/\omega_A = 0$, 1×10^{-3}, 3×10^{-3} and 5×10^{-3}, where ω_A is the toroidal Alfvén frequency.

Two different current profiles have been used in Figs. 1 and 2. That shown in Fig. 1(a) will be referred to as *rounded* and the one in 2(a) as *flattened* with *low central shear*.

According to Figs. 1 and 2, the marginal β_p is typically between 0.1 and 0.2, which is significantly lower than the 'standard' value $\beta_p = 0.3$ [7]. In trying to understand the reason for the deviation from the traditional result, we found that the important difference between the numerical computations and the large aspect ratio theory of Bussac et al [7] is *not* the finite aspect ratio but rather the *boundary conditions.*

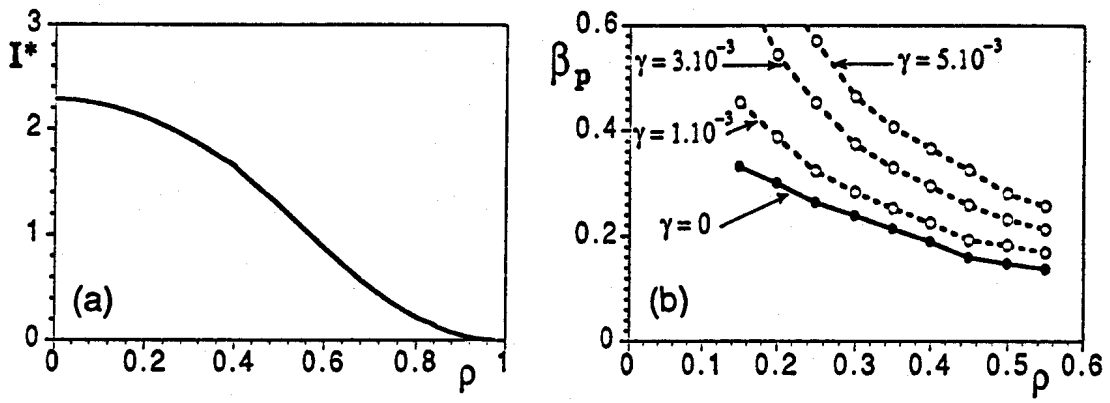

Figure 1. Circular equilibrium with a rounded current profile. (a) Surface averaged toroidal current density I (b) β_p (poloidal beta at q = 1) vs. $\rho_{q=1}$ for different growth rates of the ideal-MHD internal kink.*

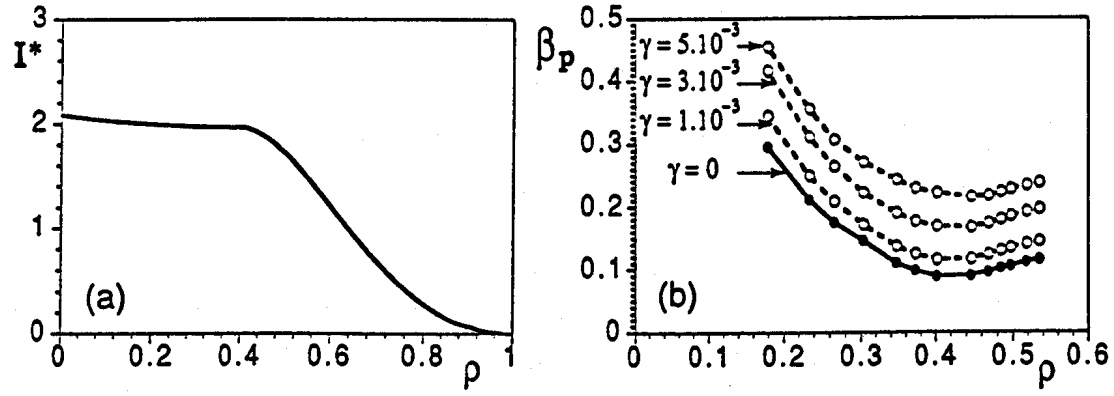

Figure 2. Circular equilibrium with flattened current profile and low central shear. (a) I(ρ) and (b) β_p vs. $\rho_{q=1}$ for different ideal-MHD growth rates.*

Bussac et al computed the critical β_p as a function of $r_{q=1}/a$, assuming a fixed plasma boundary. The assumption of a fixed boundary implies that the m = 2 side-band is wall stabilized whenever $q_a < 2$. For the parabolic current profile studied in [7], $q_a/q_0 = 2$, which means that $q_a < 2$ as soon as $q_0 < 1$, i.e., in all cases of interest for the internal kink. Evidently, the fixed boundary results for the parabolic profile refer to the case of very-low-q operation, $q_a < 2$, with a close-fitting wall. Although tokamaks can be operated this way,

the standard operating regime is $q_a > 2$, and as we will see, this affects the internal kink stability.

Figure 3 shows the β_p-limit obtained from the large aspect ratio theory using (a) a fixed boundary and (b) boundary conditions appropriate for $q_a > 2$, with the $q = 2$ surface inside the conducting plasma. [Thus, if $q_a < 2$, we add a region of currentless but perfectly conducting plasma that extends to the $q = 2$ surface at $r/a = (2/q_a)^{1/2}$. In this case, "a" denotes the radius of the current channel, not the plasma radius.] We consider three different current profiles: two polynomial profiles,

$$j(r) = \begin{cases} j_0(1 - r^2/a^2)^\ell & , \quad r < a \\ 0 & , \quad r > a \end{cases} \qquad (1)$$

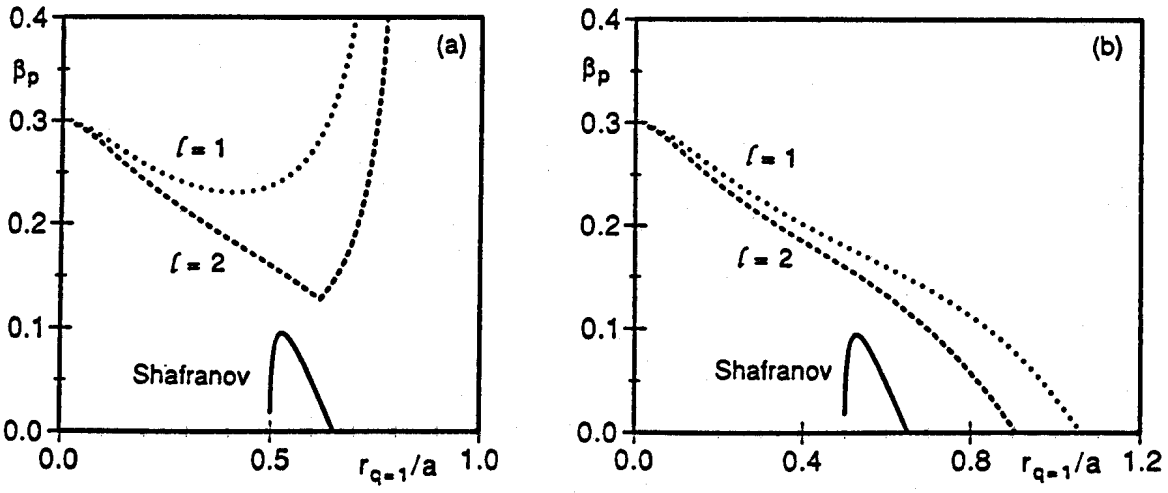

Figure 3. Marginal β_p from large aspect ratio theory for different current profiles. (a) with a rigid wall at r = a and (b) with conducting plasma extending to the q = 2 surface.

with $\ell = 1, 2$ (*parabolic* and *parabolic-squared*), for which $q_a = (\ell + 1)q_0$, and a step function, or *Shafranov* profile, with the step in the current density at $r = r_0 = 0.5$ a. For the two smooth profiles (1), the β_p-limit in Fig 3(b) falls monotonically when the $q = 1$ radius increases. This is in clear contrast to the fixed boundary result in Fig. 3(a) for the parabolic profile, where the stabilization by the wall at r = a becomes stronger with increasing $q = 1$ radius, and the pressure limit even goes to infinity for $r_{q=1}/a > 0.79$. With the modified treatment of the wall, we find limits typically in the range of 0.1 to 0.2, in good agreement

with the numerical result at aspect ratio 4 in Figs. 1 and 2.

Figure 3(b) shows that the β_p-limit goes to zero for q_0 below some profile-dependent threshold, ranging from 0.40 for the parabolic-squared profile to 0.58 for the Shafranov profile. For q_0 close to unity, the pressure limit is highly sensitive to the current profile: the Shafranov profile supports much lower pressures than the rounded-off current profiles (1).

3. IDEAL STABILITY - SHAPING EFFECTS

Previous studies of the internal kink mode in shaped cross sections give rather contradictory results. In a numerical study, Berger et al [20] found strong destabilization by ellipticity, whereas Connor and Hastie [21], using a large aspect ratio expansion, found that elliptic shaping has only a weak effect, in particular at low shear. Our numerical computations [16, 17] confirm the strong destabilizing effect, and indicate that the destabilization is connected to interchange instability. This effect was ruled out by the ordering scheme of the large aspect ratio expansion applied in [21].

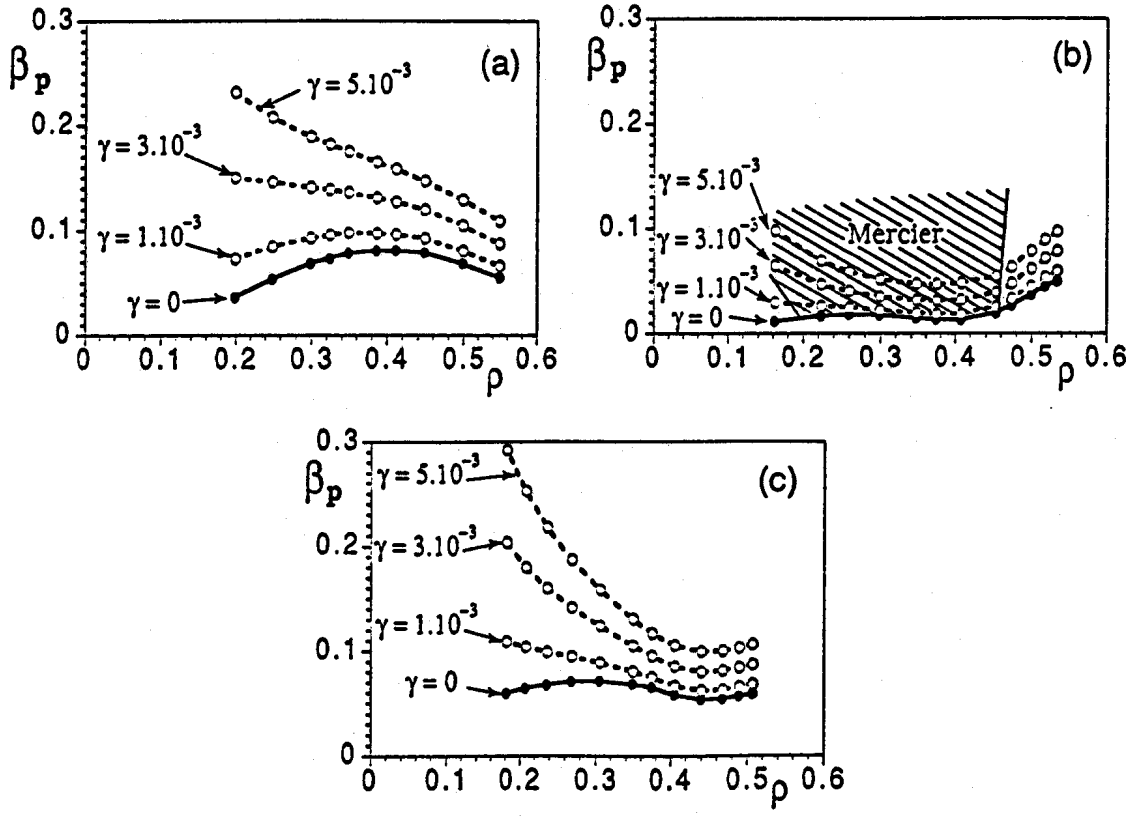

Figure 4. β_p vs. $\rho_{q=1}$ for different ideal-MHD growth rates in JET-shaped equilibria. The current profiles are: (a) rounded, (b) flattened with low central shear and (c) flattened with medium central shear.

For our numerical examples, we have chosen JET geometry: aspect ratio $R_0/a = 2.7$, elongation $\kappa = 1.7$ and triangularity $\delta = 0.3$. We used the same current profiles as for the circular examples (rounded, and flattened with low central shear), and in addition one flattened profile with twice the central shear of that in Fig. 2. This profile will be called *flattened* with *medium central shear*. The numerical stability results are shown in Fig. 4. The β_p-limits are significantly lower than in a circle, and generally lie between 0.02 and 0.1. The lowest limits occur for the flattened low-shear profile, with the weakest central shear. For this equilibrium, the onset of ideal instability largely coincides with violation of the Mercier criterion at $q = 1$, as marked in Fig. 4(b).

The numerical results give a clearly different picture than the large aspect ratio theory of [21, 22], which indicated that the destabilization from ellipticity is weak at low shear. The source of the discrepancy can be seen from the dependence on the shear of various terms in the potential energy δW, and to be explicit, we cite some analytic large aspect ratio results for the Shafranov current profile [22]. In [22], δW was written as

$$\delta W = \frac{\pi^2}{2} |\xi|^2 R_0 B_T^2 \varepsilon^2 [\, \varepsilon^2 P_T(\beta_p) + P_{ellipse} \,] \quad , \tag{2a}$$

where P_T is the usual toroidal term evaluated according to Ref. [7]:

$$P_T(\beta_p) = -\frac{1}{q_0^2 + 4(1-q_0)} \{ [2(2\beta_p - \log q_0)^2 + \log q_0] [q_0^2 + 2(1-q_0)] + (12\beta_p - \tfrac{9}{4})(1-q_0) \} = -8\beta_p^2 + (1-q_0)(\tfrac{13}{4} - 20\beta_p + 16\beta_p^2) + O((1-q_0)^2) \quad . \tag{2b}$$

The destabilizing, elliptic shaping term was evaluated using the theory of Edery et al [23] for zero pressure and infinite aspect ratio:

$$P_{ellipse} = -144\, e^2 \left(\frac{1 - q_0^2}{1 + q_0^2} \right)^2 \frac{(6 - 3q_0 + q_0^3)}{(3-q_0)^2(6+q_0)} = -\frac{144 e^2}{7} (1-q_0)^2 + O((1-q_0)^3) \quad . \tag{2c}$$

In (2), $\varepsilon = r_{q=1}/R_0$ and $e = (\kappa_{q=1} - 1)/2$ are the inverse aspect ratio and ellipticity of the $q = 1$ surface, and $q_a > 3$ has been assumed. Note that the stabilizing term in P_T varies as $1-q_0$ and that $P_{ellipse}$ is proportional to $(1-q_0)^2$. Thus, (2) indicates that the effect of ellipticity

vanishes as $q_0 \to 1$. However, it is clear that any contribution that does not vanish with $1-q_0$ (even if it is 'small' in the sense of a large aspect ratio expansion) could become important at low shear. Such terms do exist at order $\varepsilon^4\beta_p e$, i.e., they depend on the interaction of finite aspect ratio, pressure gradients and ellipticity. Because of the heavy algebra, we have refrained from trying to obtain explicit expressions as (2b,c) for the terms of this order in δW. However, the effect can be seen with less effort from a large aspect ratio expansion of the Mercier criterion [16, 17]. The flux surfaces are assumed to have the shape

$$\begin{aligned} R &= R_0 - \varepsilon\,[r - e\,E(r)]\cos\omega - \varepsilon^2\Delta(r) + \varepsilon^2\,T(r)\cos 2\omega + O(\varepsilon^3 R_0), \\ Z &= \quad \varepsilon\,[r + e\,E(r)]\sin\omega \quad\quad + \varepsilon^2\,T(r)\sin 2\omega + O(\varepsilon^3 R_0), \end{aligned} \tag{3}$$

where E and T are related to the ellipticity and triangularity by $E(r) = re$ and $T(r) = r\delta/4$, and Δ is the Shafranov shift. We now treat ε and e as *independent* small parameters and expand the Mercier criterion to second order in ε and first order in e, keeping contributions of order $\varepsilon^2 e$. At this order, the criterion for ideal interchange stability reads:

$$\begin{aligned} -D_I = \frac{1}{4} + \frac{2p'}{rB^2}\frac{q^2}{q'^2}\Big[1 - q^2 + \frac{3q^2}{4}\Big(\frac{E}{r} + E'\Big) + \frac{3q^2}{2}\Lambda\Big(\frac{E}{r} - E'\Big) \\ - \frac{R_0 q^2}{r}\Big(\frac{2ET}{r^2} + \frac{6E'T}{r} + \frac{7ET'}{2r} - \frac{3}{2}E'T'\Big)\Big] > 0, \end{aligned} \tag{4a}$$

where prime denotes differentiation with respect to r, $\Lambda \equiv R_0\,\Delta'/r \approx \beta_p(r) + \ell_i(r)/2$, and $\ell_i(r)$ is the internal inductance. An approximation of (4a) that is useful for the internal kink mode is obtained by considering almost flat current profiles with q' small and e(r) and $\delta(r)/r$ and $\beta_p(r)$ constant (parabolic pressure profile). Together with $q = 1$, this gives

$$-D_I \approx \frac{1}{4} - \frac{6\varepsilon^2 e\beta_p}{s^2}\Big(1 - \frac{2\delta}{\varepsilon}\Big) \tag{4b}$$

where $s = d(\log q)/d(\log r)|_{q=1}$.

Equation (4b) shows that ellipticity destabilizes interchange modes. This

destabilization is pronounced at low shear, and the marginal β_p can take arbitrarily low values if the shear is reduced on q = 1. [In addition, ellipticity is destabilizing at high shear independent of pressure, as shown by (2c).] The numerical examples in Fig. 4 indicate that the low-shear, finite pressure effect is generally the more important effect. Typical values of $\beta_{p,crit}$ are in the range of 0.02 to 0.1 for the JET cross section.

4. RESISTIVE STABILITY

In the limit of infinite aspect ratio, $\varepsilon \rightarrow 0$ (with p = 0 and circular boundary), the ideal kink is marginally stable and strongly unstable resistively (the resistive kink mode [9]). Toroidicity is stabilizing, and at finite aspect ratio the resistive kink with $\Delta' = \infty$ turns into a tearing mode with Δ' finite [8] (if $\beta_p < \beta_{p,crit}$ for the ideal mode). Even the resistive mode can be stabilized, $\Delta' < 0$, if the shear is sufficiently small at the q = 1 surface [2, 10]. Examples of this are shown in Fig. 5, for the flattened current profile, zero pressure and fixed boundary. The filled symbols represent equilibria with low central shear ($s_{q=1} \approx 0.04$) and the open symbols represent moderate central shear ($s_{q=1} \approx 0.07$). The figure shows that finite aspect ratio and low shear are stabilizing and that complete resistive stability can be achieved for pressureless equilibria.

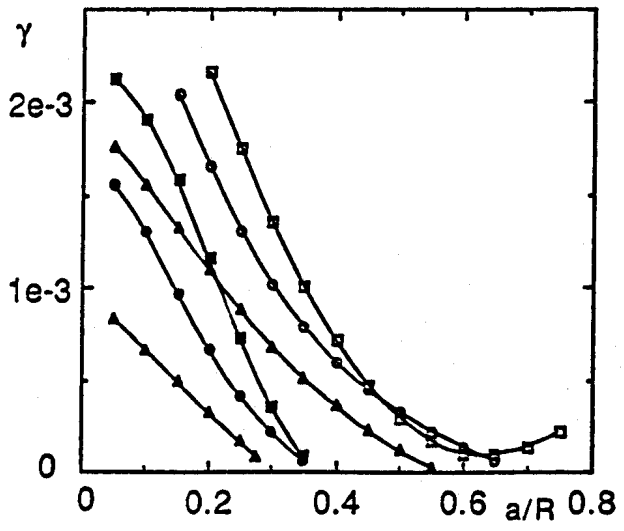

Figure 5. Resistive growth-rates at $S = 10^6$ vs. inverse aspect ratio for pressureless equilibria with flattened current profiles and low (filled symbols) or medium central shear (open). Circles indicate circular, triangles JET-shaped and squares elliptic cross section ($\kappa = 1.7$).

We find that the resistive mode is generally strongly destabilized by central pressure gradients. This takes place by two mechanisms: global effects which change Δ' and local

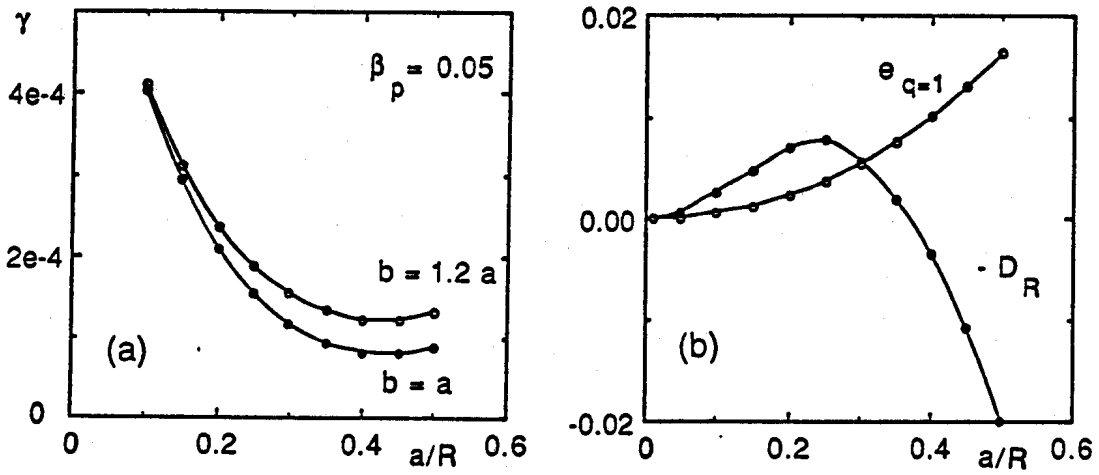

Figure 6. Resistive stability results for a circular equilibrium with $\beta_p = 0.05$, flattened current profiles and low central shear. (a) Growth rates at $S = 10^7$, and (b) resistive interchange parameter $-D_R$ and ellipticity of $q = 1$ surface vs. inverse aspect ratio.

effects which affect the resistive interchange stability at q = 1. Figures 6 - 8 show some examples where the interchange effect is important. Figure 6(a) shows the growth rate of a resistive mode for a low-shear equilibrium with circular boundary and $\beta_p = 0.05$. The current profile is identical to the low shear profile in Fig. 5, and the pressure is well below the ideal threshold. However, unlike the pressureless case, the resistive mode is not completely stabilized at low aspect ratio. The cause of the instability at low aspect ratio can be seen in Fig. 6(b); the resistive interchange criterion is violated at q = 1. The main reason for this is the slight 'natural' ellipticity of the q = 1 surface (proportional to ε^2 for a circular boundary). The importance of the resistive interchange criterion on resistive stability can be seen from the dispersion relation of Glasser, Greene and Johnson [24] (which we quote here in its simplified cylindrical form):

$$\Delta' = \frac{2\pi}{L_R} \frac{\Gamma(3/4)}{\Gamma(1/4)} Q^{5/4} \left(1 - \frac{\pi D_R}{4Q^{3/2}}\right) , \qquad (5)$$

where $L_R = aS^{-1/3}$ is the resistive layer width of the interchange ordering and $Q = \gamma\tau_A S^{1/3}$ is the normalized growth rate.

According to (5), the stability of resistive modes at high S becomes almost entirely

determined by the resistive interchange parameter. If the criterion is violated, $-D_R < 0$, there is always an unstable mode (for arbitrary Δ' and S), and for large S its growth rate scales as $S^{-1/3}D_R^{2/3}$. On the other hand, if resistive interchanges are stable, $-D_R > 0$, tearing modes remain stable for Δ' less than some positive threshold Δ'_{crit}, which scales as $S^{1/3}(-D_R)^{5/6}$. We emphasize that, at high S, Δ'_{crit} becomes large, and the stability of resistive modes is completely dominated by the resistive interchange criterion. For q = 1, and with the same approximations as in (4b), the resistive interchange parameter is given by

$$-D_R \approx \frac{2\varepsilon^2\beta_p}{s^2}\left[2s\Lambda - 3e\left(1 - \frac{2\delta}{\varepsilon}\right)\right] \quad . \tag{6}$$

Another illustration of the important role played by interchange stability is given in Fig. 7. This equilibrium has the same pressure and I* profiles as that in Fig. 6, but the plasma boundary is oblate, $\kappa = 0.9$. The q = 1 surface remains oblate at low aspect ratio and resistive interchanges are stable at q = 1. As the aspect ratio decreases, the growth rate first decreases, then becomes complex and finally the mode is completely stabilized, as predicted by the theory of Glasser et al [24].

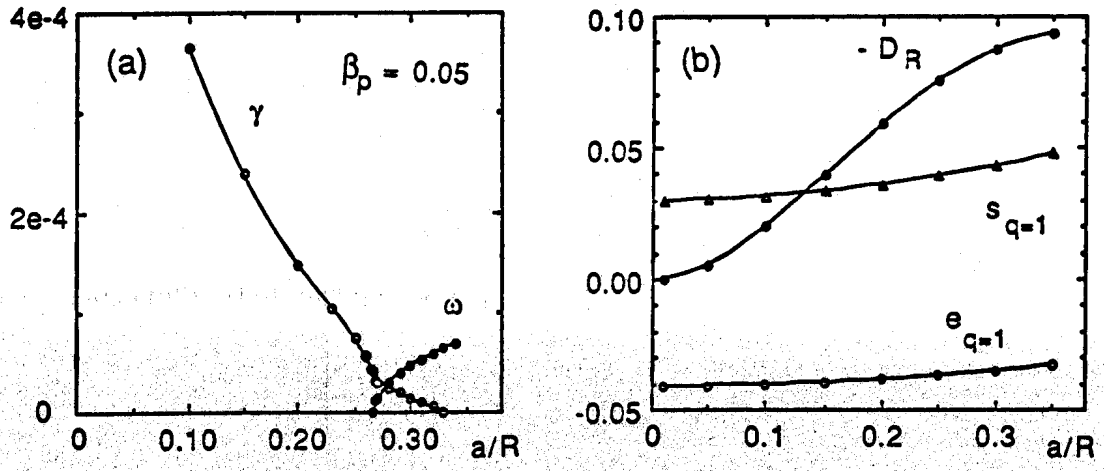

Figure 7. Resistive stability results for an oblate boundary, $\kappa = 0.9$, and the same profiles as in Fig. 6. (a) Growth rates at $S = 10^7$ (note complex γ and stabilization at low aspect ratio) and (b) resistive interchange parameter $-D_R$, shear and ellipticity at the q = 1 surface.

For a JET-shaped cross section ($\kappa = 1.7$, $\delta = 0.3$) the dependence on aspect ratio is more complicated, see Fig. 8. The interchange effects are stabilizing at large aspect ratio (where the triangularity term is dominant in D_R, see Eq. (6)) and destabilizing for $a/R_0 >$

0.14 (where the ellipticity term is dominant). For $a/R_0 > 0.22$, the destabilization by ellipticity is strong enough to drive the mode ideally unstable, $-D_I < 0$.

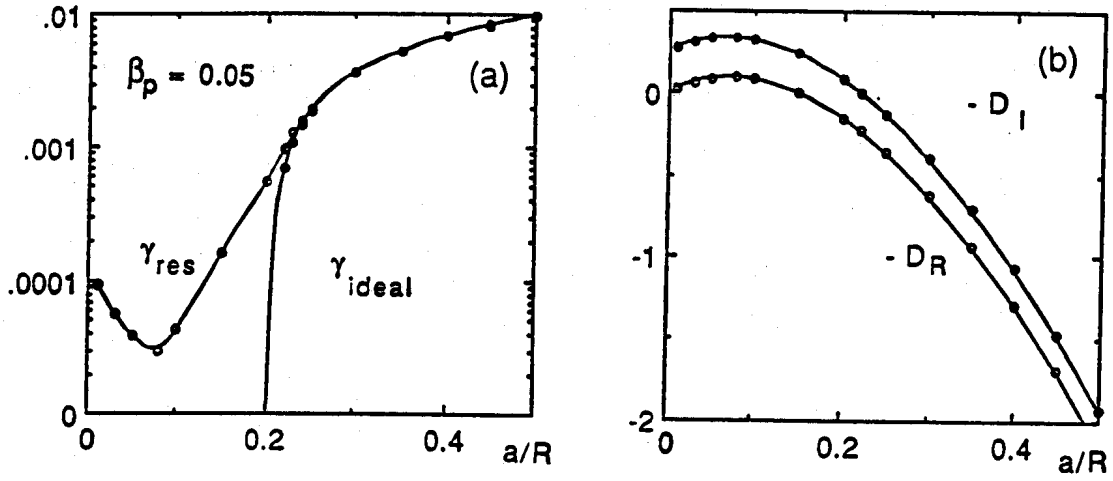

Figure 8. Stability results for a JET-shaped boundary and the same profiles as in Fig. 6. (a) Ideal (solid circles) and resistive growth rates at $S = 10^7$ (open circles) and (b) ideal, $-D_I$, and resistive, $-D_R$, interchange parameters at the $q = 1$ surface.

5. CURRENT PROFILE EFFECTS

It is generally thought that the triggering of sawtooth crashes is more closely connected to changes in the current profile than to the central pressure. To examine the influence of the current profile on the resistive internal kink, we have used the same method as in Secs. 2-3; a profile is specified for the surface averaged toroidal current density $I^*(\Psi)$, leaving free a multiplicative factor that is adjusted to specify the $q = 1$ radius. Results will be shown here for two profiles, the flattened low-shear profile (see Fig. 2) and one profile where the I^* has shoulders, giving rise to a pronounced, local flattening of the q-profile. We refer to this profile as the *TEXTOR* profile [2]. The two q-profiles are shown together with stability results for circular plasma boundary in Figs. 9 and 10. Here, resistive growth rates at different S-numbers are plotted vs. the parameter q_p, which is the q-value at the point of minimum shear, $\rho \approx 0.4$. A conducting wall is assumed at radius $r = 1.2a$.

Figure 9 shows that the low shear profile is never completely resistively stable. Nevertheless, the growth rates can be very small and obey the resistive tearing mode scaling

when β_p is small and $q_p > 1$, i.e., when the q = 1 surface is in the inner region of low shear. Pressure driven, and at least partly ideal, instabilities become prominent when $q_p \leq 1$ and the q = 1 surface approaches the outer, high shear region. If we assume that weak resistive instabilities are stabilized during the ramp phase of the sawteeth by kinetic effects or by nonlinearity, such instabilities, whose main driving energy is pressure, but whose growth rates are sensitive to small changes in the current profile, give one possible explanation for how the crashes might be triggered. During the ramp phase, the q-values in the central region are decreasing with time and the q = 1 surface moves outward (as seen, e.g., from observations of 'snakes' which follow the q = 1 surface [3]). When the q = 1 surface approaches the outer region of higher shear, the internal kink mode eventually becomes sufficiently unstable to trigger a sawtooth crash.

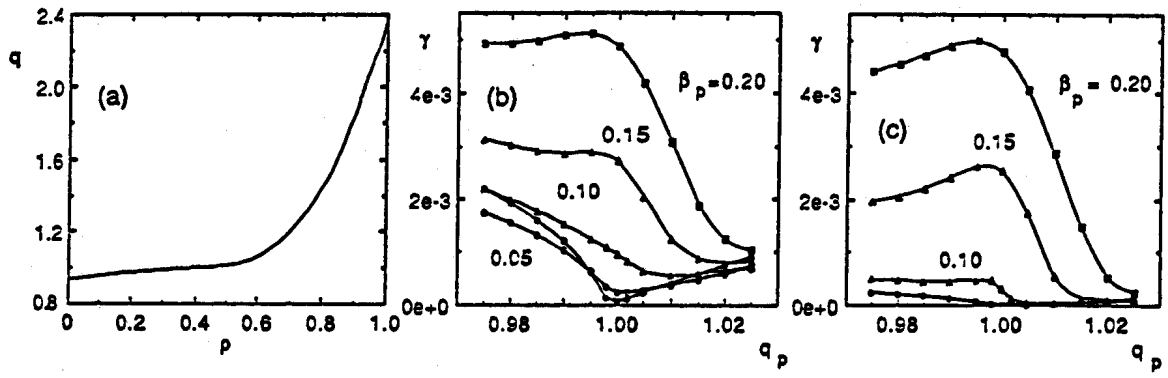

Figure 9. Current profile dependence for circular equilibrium with low central shear. (a) q-profile. (b,c) Resistive growth-rates vs. q_p (q at minimum shear, $\rho \approx 0.4$) for (b) $S = 6 \times 10^6$ and (c) $S = 6 \times 10^8$.

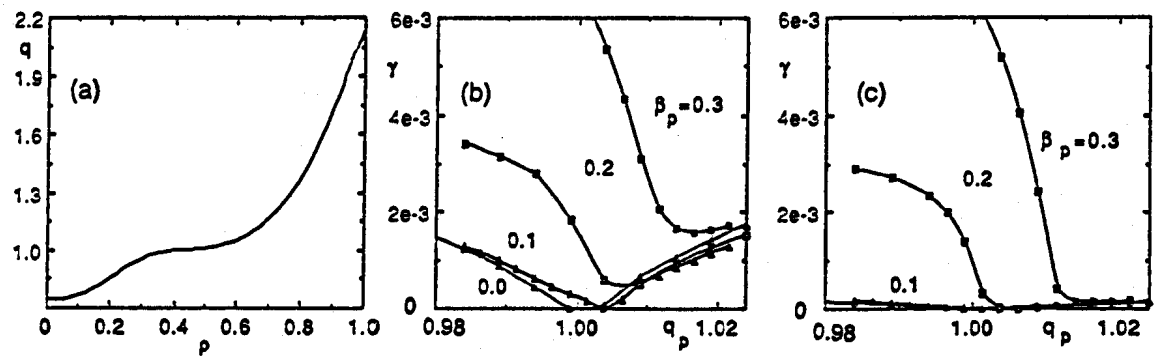

Figure 10. Current profile dependence for circular equilibrium with TEXTOR profile. (a) q-profile. (b,c) Resistive growth-rates vs. q_p (q at minimum shear, $\rho \approx 0.4$) for (b) $S = 6 \times 10^6$ and (c) $S = 6 \times 10^8$.

The TEXTOR profile gives qualitatively similar results, see Fig. 10, although

generally this profile is more stable. For instance, the threshold in β_p for ideal instability is about twice that for the low shear profile. Figure 10 confirms the results of [2] that there is an interval in q_p where the TEXTOR profile is completely stable. However, the stable window is small; its width in terms of q_p is about $\Delta q_p \approx 0.005$ at zero pressure, and the window closes completely at $\beta_p \approx 0.10$.

Of course, experimentally, the central region remains macroscopically stable during the ramp phase of the sawteeth, and by comparison with Figs. 9 and 10, it appears that the requirement of linear resistive MHD stability is too stringent. It is possible that weakly unstable resistive MHD modes are stabilized during the ramp phase by kinetic effects and/or nonlinearity. This view is supported by the even more pessimistic resistive MHD stability results obtained for JET geometry [16].

6. CONCLUSION

Detailed studies of the internal kink mode have revealed several new effects. Generally, we find the mode more unstable than previously assumed. Typical ideal stability limits in poloidal beta at the $q = 1$ surface are of the order of 0.1 to 0.2 for circular equilibria. For elliptically shaped equilibria, the limits are significantly lower; typical values range from 0.02 to 0.1, but arbitrarily low limits can result if the shear is reduced in the $q \leq 1$ region. The destabilization by ellipticity is particularly strong for low central shear and can be correlated with interchange instability.

Concerning resistive stability, we find that although low shear is stabilizing at zero pressure, it tends to be destabilizing even for very modest central pressure gradients because of interchange instability. This effect is strong for elliptic shaping (including JET shape) which makes the averaged curvature on $q = 1$ unfavorable. For JET shape, we have found no case with $\beta_p \geq 0.05$ that is resistively stable, and complete resistive stability with free boundary was found only for current profiles of the TEXTOR type with shoulders. Stabilization for the TEXTOR profile requires a very careful tuning of parameters, e.g., specification of q with a precision of half a percent.

We tentatively conclude that the requirement of resistive MHD stability is overly pessimistic for the internal kink. It appears likely that the resistive internal mode is

stabilized during the ramp phase of the sawteeth by kinetic effects such as diamagnetic rotation or trapped particles, or may be nonlinearly saturated. Work is underway to incorporate certain kinetic effects in the MARS code.

Acknowledgement: This work was funded in part by the Swiss National Science Foundation.

REFERENCES

1. S. von Goeler, W. Stodiek and N. Sauthoff, Phys. Rev. Lett. **33**, 1201 (1974).
2. H. Soltwish, W. Stodiek, J. Manickam and J. Schlüter, in Proceedings of the 11th International Conference, Kyoto (IAEA, Vienna, 1987), Vol. 1, p. 263.
3. A. Weller, et al, Phys. Rev. Lett. **59**, 2303 (1987).
4. K. McCormick, A. Eberhagen, H. Murmann and the ASDEX Team, in Proceedings of the 15th European Conference, Dubrovnik, 1988, Vol 12B, Part I, p. 35.
5. D.J. Campbell, et al, Phys. Rev. Lett. **60**, 2148 (1988).
6. B.B. Kadomtsev, Sov. J. Plasma Phys. **1**, 389 (1975) [Fiz. Plasmy **1**, 710 (1975)].
7. M.N. Bussac, R. Pellat, D. Edery and J. Soulé, Phys. Rev. Lett. **35**, 1638 (1975).
8. M.N. Bussac, R. Pellat, D. Edery, and J. Soulé, in Proceedings of the 6th International Conference, Berchtesgaden (IAEA, Vienna, 1977), Vol. 1, p. 607.
9. B. Coppi, R. Galvao, R. Pellat, M. Rosenbluth and P. Rutherford, Sov. J. Plasma Phys. **2**, 533 (1976).
10. J.A. Holmes, B.A. Carreras, and L.A. Charlton, Phys. Fluids **B1**, 788 (1989).
11. R.B. White, et al, Phys. Rev. Lett. **60**, 2038 (1988); ibid. **62**, 539 (1989).
12. G. Vlad and A. Bondeson, Nucl. Fusion **29**, 1139 (1989).
13. W. Park and D.A. Monticello, Nucl. Fusion **30**, 2413 (1990).
14. J.A. Wesson, Nucl. Fusion **30**, 2545 (1990).
15. J.F. Drake and R.G. Kleva, Phys. Rev. Lett. **66**, 1458 (1991).
16. A. Bondeson, G. Vlad and H. Lütjens, Phys. Fluids **B4**, 1889 (1992).
17. H. Lütjens, A. Bondeson and G. Vlad, LRP 446/91, to appear in Nucl. Fusion 1992.
18. H. Lütjens, A. Bondeson and A. Roy, Comput. Phys. Commun. **69**, 287 (1992).
19. A. Bondeson, G. Vlad, and H. Lütjens, in Proceedings of the IAEA Technical Committee Meeting on *Advances in Simulation and Modelling of Thermonuclear Plasmas*, Montréal, Canada, 1992.
20. D. Berger, L.C. Bernard, R. Gruber and F. Troyon, in Proceedings of the 6th International Conference, Berchtesgaden (IAEA, Vienna, 1977), Vol. 2, p. 411.
21. J.W. Connor and R.J. Hastie, Culham report CLM-M-106 (1985).
22. A. Bondeson and M.-N. Bussac, Nucl. Fusion **32**, 513 (1992).
23. D. Edery, G. Laval, R. Pellat and J.L. Soulé, Phys. Fluids **19** (1976) 260.
24. A.H. Glasser, J.M. Greene and J.L. Johnson, Phys. Fluids **18**, 875 (1975).

MHD STABILITY IN 3D ANISOTROPIC PRESSURE PLASMAS

W. Anthony Cooper

Centre de Recherches en Physique des Plasmas,
Association Euratom-Confédération Suisse,
Ecole Polytechnique Fédérale de Lausanne,
Lausanne, Switzerland

1. Introduction

Auxiliary heating methods such as neutral beam injection and radio frequency heating that are employed to raise the temperature in magnetically confined plasmas also induce anisotropy in the plasma pressure. This is particularly evident in the low density hot ion mode of operation. A detailed experimental study of the impact of 1 MW of tangential neutral beam injection at an energy of 40 Kev has been reported in the Compact Helical System (CHS) in Nagoya, Japan [1]. This device is a low aspect ratio ($A \simeq 5$) torsatron that is fully three dimensional (3D) in character. Pressure anisotropy levels in which $p_{||}/p_{\perp} \simeq 3$ have been measured. This motivates us to formulate the linear magnetohydrodynamic (MHD) stability problem in 3D plasma confinement configurations in which the parallel pressure $p_{||}$ differs from the perpendicular pressure $p_{\perp}$. The anisotropic pressure 3D MHD equilibrium problem has already been investigated [2] and a version of the 3D MHD equilibrium code VMEC [3] has been appropriately modified to account for $p_{||} \neq p_{\perp}$.

The MHD stability in anisotropic pressure stellarator devices has been examined previously by Buckle et al. [4]. They follow an initial value approach based on the double adiabatic model in an Eulerian grid and adopt a large aspect ratio expansion. The underlying equilibrium, however, is not fully selfconsistent because $p_{||}$ and $p_{\perp}$ are chosen arbitrarily as functions of the radial variable only. Although this violates the constraint imposed by parallel force balance, their applications to several different stellarator devices represent a very useful first step in the quantification of the impact of pressure anisotropy on the MHD stability properties in such configurations. Alternatively, the energetic particle species that drive the pressure anisotropy can be considered as a rigid noninteracting current layer. The global and local MHD equations that govern the linear stability properties in such a limit have been described by Cooper [5]. The corresponding Mercier criterion in a helically symmetric stellarator with a helical axis and circular cross section has been evaluated by Miller [6]. This model yields more optimistic stability criteria than the fully fluid model. A model by Rosenbluth et al. [7] that includes a kinetic response of the fast particles is shown to yield a more stabilising criterion for localised Mercier modes as long as the drifts of the energetic particles do not reverse [8]. Therefore, under conditions in which drift reversal is absent the fully fluid and rigid models invoked for the investigation of

the MHD stability of plasmas can be considered as two limits that yield conservative estimates in the determination of operational boundaries of magnetically confined devices with anisotropic energetic particle layers.

In this paper, we formulate the linear 3D MHD stability problem variationally for anisotropic pressure plasmas in the fully fluid limit from the Kruskal-Oberman energy principle [9]. The 3D equilibrium state is constrained to have nested magnetic flux surfaces with a single magnetic axis. Magnetic island structures and questions of the existence of 3D equilibria are excluded from the formulation. We apply the Boozer magnetic coordinate system (s, θ, ϕ) [10], appropriately modified for anisotropic plasmas [5]. The radial variable s labels the magnetic surfaces, while θ and ϕ correspond to the periodic poloidal and toroidal angular variables, respectively. In these coordinates, the magnetic field in the contravariant representation is $\mathbf{B} = \nabla\phi\times\nabla\Psi + \nabla\Phi\times\nabla\theta$, where $\Psi(s)$ and $\Phi(s)$ are the poloidal and toroidal magnetic flux functions, respectively. In the covariant representation, the magnetic field can be described as $\sigma\mathbf{B} = \sigma B_s \nabla s + J(s)\nabla\theta - I(s)\nabla\phi$, where $\sigma > 0$ is the firehose stability parameter that characterises anisotropic plasmas, while $J(s)$ and $I(s)$ constitute the effective toroidal and poloidal current flux functions, respectively, derived from the relation $\mathbf{K} = \nabla\times(\sigma\mathbf{B})$. In order to tackle the global stability problem, we Fourier decompose the perturbed displacement vector in the periodic angular variables and apply a finite element discretisation scheme in the radial coordinate to reduce the problem to a special block pentadiagonal matrix eigenvalue equation. This equation is amenable to solution with an inverse vector iteration method. The local stability is investigated through the application of the ballooning representation within the covering space concept [11], from which we derive the ballooning mode equation. It is worthy to note that we can express the geodesic magnetic curvature in terms of the derivative along the magnetic field lines of the effective parallel current density function $\mathbf{K}\cdot\mathbf{B}/B^2$. This quantity, in turn, can be very efficiently calculated from a magnetic differential equation in the Boozer coordinates. With this form for the geodesic curvature, the asymptotic analysis of the ballooning equation yields a closed form for the Mercier criterion which is practical and straightforward to evaluate and agrees with the expression previously derived by Johnson and Hastie in Hamada coordinates [12].

2. Global MHD Stability

Prior to outlining the derivation of the equations that govern the global stability in 3D magnetofluids, we note that the covariant radial magnetic field can be calculated from the radial force balance relation, namely

$$(\sqrt{g}\mathbf{B}\cdot\nabla)(\sigma B_s) = \sqrt{g}\frac{\partial p_{\|}}{\partial s}\bigg|_B + \left[\Psi'(s)J'(s) - \Phi'(s)I'(s)\right], \tag{1}$$

and correspondingly the parallel current density function is

$$\frac{\mathbf{K}\cdot\mathbf{B}}{B^2} = \frac{[J(s)I'(s) - I(s)J'(s)]}{(\sigma\sqrt{g}B^2)} + \frac{1}{(\sigma\sqrt{g}B^2)}\left[I(s)\frac{\partial(\sigma B_s)}{\partial\theta} + J(s)\frac{\partial(\sigma B_s)}{\partial\phi}\right]. \tag{2}$$

This procedure highlights the singular nature of the parallel current density on rational magnetic surfaces in 3D configurations. These singular current sheets constitute an important source of free energy for instabilities within the MHD model.

The investigation of the linear MHD stability in a 3D fully interacting fluid can be formulated variationally from the aplication of the universal term of the Kruskal-Oberman energy principle in which the positive-definite kinetic energy integral is ignored [9]. The energy principle can be expressed as [13]

$$\delta W_u = \frac{1}{2}\int\int\int d^3x\left\{\sigma Q_\perp^2 + \tau Q_\parallel^2 + 2\mathbf{Q}\cdot\left[\frac{(\mathbf{K}\times\nabla s)}{|\nabla s|^2} + \left(\frac{\partial p_\parallel}{\partial s}\bigg|_B - \frac{\partial p_\perp}{\partial s}\bigg|_B\right)\frac{\mathbf{B}}{B^2}\right](\xi^s\right. \tag{3}$$
$$\left. + \left[\frac{(\mathbf{K}\times\nabla s)\cdot\nabla\times(\mathbf{B}\times\nabla s)}{|\nabla s|^4} + \frac{1}{|\nabla s|^2}\frac{\partial p_\parallel}{\partial s}\bigg|_B(\nabla\cdot\nabla s) + \frac{1}{2}\left(\frac{\partial p_\parallel}{\partial s}\bigg|_B - \frac{\partial p_\perp}{\partial s}\bigg|_B\right)\frac{\nabla s\cdot\nabla B^2}{B^2|\nabla s|^2}\right](\xi^s)^2\right\},$$

where the perturbed displacement vector is ξ, $\xi^s \equiv \xi\cdot\nabla s$, the perturbed magnetic field is $\mathbf{Q} = \nabla\times(\xi\times\mathbf{B})$ and $\tau = 1 + (\partial p_\perp/\partial B)/B > 0$ is the mirror stability criterion parameter. We decompose ξ as

$$\xi = \sqrt{g}\xi^s\nabla\theta\times\nabla\phi + \eta\frac{\mathbf{B}\times\nabla s}{B^2} + \left[\frac{J(s)}{\Phi'(s)\sigma B^2}\eta - \mu\right]\mathbf{B}. \tag{4}$$

It is straightforward to demonstrate that the component μ of the perturbation does nor enter the problem. The last term in the energy principle constitutes the basic instability driving term and can be expressed as

$$\sqrt{g}D = \frac{\partial p_\parallel}{\partial s}\bigg|_B\frac{\partial\sqrt{g}}{\partial s} - \left[\Psi'(s)\Phi''(s) - \Phi'(s)\Psi''(s)\right]\frac{\mathbf{K}\cdot\mathbf{B}}{B^2} - \frac{[J(s)\Psi''(s) - I(s)\Phi''(s)]}{(\sigma\sqrt{g}B^2)}\sqrt{g}\frac{\partial p_\parallel}{\partial s}\bigg|_B \tag{5}$$
$$-(\sqrt{g}\mathbf{B}\cdot\nabla)\left\{\left[I(s)\frac{g_{s\theta}}{\sqrt{g}} + J(s)\frac{g_{s\phi}}{\sqrt{g}}\right]\frac{\mathbf{K}\cdot\mathbf{B}}{|\nabla s|^2\sigma^2B^2} + \frac{B_s}{B^2}\frac{\partial p_\parallel}{\partial s}\bigg|_B\right\} + \sqrt{g}\left(\frac{\partial p_\parallel}{\partial s}\bigg|_B - \frac{\partial p_\perp}{\partial s}\bigg|_B\right)\frac{1}{2B^2}\frac{\partial B^2}{\partial s},$$

after invoking some useful equilibrium relations that pertain to the Boozer magnetic coordinates [5]. We expand the perpendicular perturbed magnetic field in the contravariant representation to determine $\sigma Q_\perp^2$ and obtain an expression for δW_u that is very similar to that derived for the rigid hot particle model [5].

Fourier decomposition of the perturbation components in the periodic angular variables is applied such that

$$\xi^s(s,\theta,\phi) = \sum_\ell s^{-q_\ell}\xi_\ell(s)\sin(m_\ell\theta - n_\ell\phi + \Delta), \tag{6}$$

$$\eta(s,\theta,\phi) = \sum_\ell \eta_\ell(s)\cos(m_\ell\theta - n_\ell\phi + \Delta), \tag{7}$$

where m_ℓ and n_ℓ represent the poloidal and toroidal mode numbers, respectively, ℓ is an index that labels the (m,n) pairs, q_ℓ is chosen to satisfy regularity conditions at the magnetic axis and Δ is a fixed arbitrary phase factor. In Fourier space, the energy principle reduces to

$$\frac{2L_s}{(2\pi)^2}\delta W_u = \frac{1}{2}\int_0^1 ds\sum_{\ell,k}\left\langle\frac{\partial\xi_\ell}{\partial s}\left[\frac{(\sigma\sqrt{g}B^2)}{s^{(q_\ell+q_k)}}C_{\ell k}^{(0)}(s)\right]\frac{\partial\xi_k}{\partial s} + \xi_\ell(s)\left[\frac{C_{\ell k}^{(9)}(s)}{s^{(q_\ell+q_k)}}\right]\xi_k(s)\right.$$
$$+\frac{\partial\xi_\ell}{\partial s}\left\{\frac{C_{\ell k}^{(2)}(s) - [m_k\Psi'(s) - n_k\Phi'(s)]C_{\ell k}^{(1)}(s) + \left[J(s)\Psi''(s) - I(s)\Phi''(s) - \frac{q_k}{s}(\sigma\sqrt{g}B^2)\right]C_{\ell k}^{(0)}(s)}{s^{(q_\ell+q_k)}}\right\}\xi_k(s)$$
$$+\xi_\ell(s)\left\{\frac{C_{\ell k}^{(2)}(s) - [m_\ell\Psi'(s) - n_\ell\Phi'(s)]C_{k\ell}^{(1)}(s) + \left[J(s)\Psi''(s) - I(s)\Phi''(s) - \frac{q_\ell}{s}(\sigma\sqrt{g}B^2)\right]C_{\ell k}^{(0)}(s)}{s^{(q_\ell+q_k)}}\right\}\frac{\partial\xi_k}{\partial s}$$
$$\left.+\frac{\partial\xi_\ell}{\partial s}\left\{\frac{[m_kI(s) - n_kJ(s)]}{s^{q_\ell}}C_{\ell k}^{(0)}(s)\right\}\eta_k(s) + \eta_\ell(s)\left\{\frac{[m_\ell I(s) - n_\ell J(s)]}{s^{q_k}}C_{\ell k}^{(0)}(s)\right\}\frac{\partial\xi_k}{\partial s}\right. \tag{8}$$

$$+\xi_\ell(s)\Bigg\{\frac{[m_k\Psi'(s)-n_k\Phi'(s)]}{s^{q_\ell}(\sigma\sqrt{g}B^2)}\left\{[m_\ell\Psi'(s)-n_\ell\Phi'(s)]\,C_{k\ell}^{(4)}(s)-(\sigma\sqrt{g}B^2)C_{\ell k}^{(5)}(s)-[\Psi'(s)\Phi''(s)-\Phi'(s)\Psi''(s)]\,C_{\ell k}^{(6)}(s)\right\}$$

$$+\frac{[m_k I(s)-n_k J(s)]}{s^{q_\ell}(\sigma\sqrt{g}B^2)}\left\{C_{\ell k}^{(2)}(s)+\left[J(s)\Psi''(s)-I(s)\Phi''(s)-\frac{q_\ell}{s}(\sigma\sqrt{g}B^2)\right]C_{\ell k}^{(0)}(s)-[m_\ell\Psi'(s)-n_\ell\Phi'(s)]\,C_{k\ell}^{(1)}(s)\right\}\Bigg\}\eta_k(s)$$

$$+\eta_\ell(s)\Bigg\{\frac{[m_\ell\Psi'(s)-n_\ell\Phi'(s)]}{s^{q_k}(\sigma\sqrt{g}B^2)}\left\{[m_k\Psi'(s)-n_k\Phi'(s)]\,C_{\ell k}^{(4)}(s)-(\sigma\sqrt{g}B^2)C_{\ell k}^{(5)}(s)-[\Psi'(s)\Phi''(s)-\Phi'(s)\Psi''(s)]\,C_{\ell k}^{(6)}(s)\right\}$$

$$+\frac{[m_\ell I(s)-n_\ell J(s)]}{s^{q_k}(\sigma\sqrt{g}B^2)}\left\{C_{\ell k}^{(2)}(s)+\left[J(s)\Psi''(s)-I(s)\Phi''(s)-\frac{q_k}{s}(\sigma\sqrt{g}B^2)\right]C_{\ell k}^{(0)}(s)-[m_k\Psi'(s)-n_k\Phi'(s)]\,C_{k\ell}^{(1)}(s)\right\}\Bigg\}\xi_k(s)$$

$$+\eta_\ell(s)\left\{\frac{[m_\ell\Psi'(s)-n_\ell\Phi'(s)][m_k\Psi'(s)-n_k\Phi'(s)]C_{\ell k}^{(6)}(s)+[m_\ell I(s)-n_\ell J(s)][m_k I(s)-n_k J(s)]C_{\ell k}^{(0)}(s)}{(\sigma\sqrt{g}B^2)}\right\}\eta_k(s)\Bigg\rangle,$$

where L_s is the number of periods of the instability structure once around the torus. For most practical applications, $L_s = 1$. The double Fourier flux tube integrals are typically of the form

$$C_{\ell k}^{(j)}(s)=\frac{2L_s}{4\pi^2}\int_0^{\frac{2\pi}{L_s}}\int_0^{2\pi}d\theta d\phi A_j(s,\theta,\phi)t_\ell(\theta,\phi)t_k(\theta,\phi), \tag{9}$$

where t_ℓ and t_k denote the trigonometric functions sine or cosine. The coefficients $A_j(s,\theta,\phi)$ are $A_0 = \tau/\sigma$, $A_1 = \tau B_s$, $A_2 = \sqrt{g}\partial p_\perp/\partial s$, $A_3 = \sigma g_{ss}/\sqrt{g} - (1-\tau/\sigma)(\sigma B_s)^2/(\sigma\sqrt{g}B^2)$, $A_4 = I(s)\sigma g_{s\theta}/\sqrt{g} + J(s)\sigma g_{s\phi}/\sqrt{g}$, $A_5 = \mathbf{K}\cdot\mathbf{B}/B^2$, $A_6 = \sigma^2|\nabla s|^2$ and

$$A_7(s,\theta,\phi)=\left.\frac{\partial p_\parallel}{\partial s}\right|_B\frac{\partial\sqrt{g}}{\partial s}-\sqrt{g}\frac{(\sigma B_s)}{(\sigma\sqrt{g}B^2)}(\sqrt{g}\mathbf{B}\cdot\nabla)\left(\left.\frac{\partial p_\parallel}{\partial s}\right|_B-\left.\frac{\partial p_\perp}{\partial s}\right|_B\right)+\sqrt{g}\left(\left.\frac{\partial p_\parallel}{\partial s}\right|_B-\left.\frac{\partial p_\perp}{\partial s}\right|_B\right)\times$$

$$\left\{\frac{1}{2B^2}\frac{\partial B^2}{\partial s}-\frac{1}{\sigma B^2}\left.\frac{\partial p_\parallel}{\partial s}\right|_B-\frac{B_s}{\sqrt{g}B^2}(\mathbf{B}\cdot\nabla)\sqrt{g}-\frac{[J(s)\Psi''(s)-I(s)\Phi''(s)+J'(s)\Psi'(s)-I'(s)\Phi'(s)]}{(\sigma\sqrt{g}B^2)}\right\}. \tag{10}$$

The product t_ℓ times t_k correponds to sine times sine for the coefficients $C_{\ell k}^{(0)}$, $C_{\ell k}^{(2)}$, $C_{\ell k}^{(5)}$, $C_{\ell k}^{(6)}$ and $C_{\ell k}^{(7)}$, and to cosine times cosine for $C_{\ell k}^{(3)}$. This set of coefficients is symmetric to index exchange. The integrand of the coefficients $C_{\ell k}^{(1)}$ and $C_{\ell k}^{(4)}$ are described with $t_\ell(\theta,\phi) = \sin(m_\ell\theta - n_\ell\phi + \Delta)$ and $t_k(\theta,\phi) = \cos(m_k\theta - n_k\phi + \Delta)$. $C_{\ell k}^{(1)}$ and $C_{\ell k}^{(4)}$ are thus nonsymmetric to index exchange. The coefficient $C_{\ell k}^{(9)}$ is a linear combination of all the other coefficients and can be written as

$$\begin{aligned}C_{\ell k}^{(9)}(s)=&\left[\Psi'(s)\Phi''(s)-\Phi'(s)\Psi''(s)\right]C_{\ell k}^{(5)}(s)+\frac{[\Psi'(s)\Phi''(s)-\Phi'(s)\Psi''(s)]^2}{(\sigma\sqrt{g}B^2)}C_{\ell k}^{(6)}(s)\\&+\frac{\left[J(s)\Psi''(s)-I(s)\Phi''(s)-\frac{q_\ell}{s}(\sigma\sqrt{g}B^2)\right]\left[J(s)\Psi''(s)-I(s)\Phi''(s)-\frac{q_k}{s}(\sigma\sqrt{g}B^2)\right]}{(\sigma\sqrt{g}B^2)}C_{\ell k}^{(0)}(s)\\&+\left\{\frac{[J(s)\Psi''(s)-I(s)\Phi''(s)]}{(\sigma\sqrt{g}B^2)}-\frac{(q_\ell+q_k)}{s}\right\}C_{\ell k}^{(2)}(s)+C_{\ell k}^{(7)}(s)\\&+[m_\ell\Psi'(s)-n_\ell\Phi'(s)][m_k\Psi'(s)-n_k\Phi'(s)]\,C_{\ell k}^{(3)}(s)\\&-[m_k\Psi'(s)-n_k\Phi'(s)]\left\{\left[\frac{\Psi'(s)\Phi''(s)-\Phi'(s)\Psi''(s)}{(\sigma\sqrt{g}B^2)}\right]C_{\ell k}^{(4)}(s)+\frac{\left[J(s)\Psi''(s)-I(s)\Phi''(s)-\frac{q_\ell}{s}(\sigma\sqrt{g}B^2)\right]}{(\sigma\sqrt{g}B^2)}C_{\ell k}^{(1)}(s)\right\}\\&-[m_\ell\Psi'(s)-n_\ell\Phi'(s)]\left\{\left[\frac{\Psi'(s)\Phi''(s)-\Phi'(s)\Psi''(s)}{(\sigma\sqrt{g}B^2)}\right]C_{k\ell}^{(4)}(s)+\frac{\left[J(s)\Psi''(s)-I(s)\Phi''(s)-\frac{q_k}{s}(\sigma\sqrt{g}B^2)\right]}{(\sigma\sqrt{g}B^2)}C_{k\ell}^{(1)}(s)\right\}.\end{aligned} \tag{11}$$

Considering that radial derivatives act solely upon $\xi_\ell(s)$ in δW_u, it is convenient to apply for example nonconforming finite hybrid elements for the radial discretisation

of the stability problem [14]. Invoking a model kinetic energy [5], the linear MHD stability problem reduces formally to a special block pentadiagonal matrix equation

$$\mathcal{A}\mathbf{x} = \lambda \mathcal{B}\mathbf{x} \tag{12}$$

where $\mathcal{A}$ is the potential energy matrix, $\mathcal{B}$ is the kinetic energy matrix, $\mathbf{x}$ is the eigenfunction, and $\lambda = \omega^2$ is the eigenvalue. This equation can be solved with an inverse vector iteration method [14].

3. Local MHD Stability

The 3D ballooning mode equation derived from the Kruskal-Oberman energy principle is [15]

$$(\mathbf{B}\cdot\nabla)\left[\sigma h^2 (\mathbf{B}\cdot\nabla\chi)\right] + (1-\lambda)h^s\left(\left.\frac{\partial p_\parallel}{\partial s}\right|_B + \frac{\sigma}{\tau}\left.\frac{\partial p_\perp}{\partial s}\right|_B\right)(\mathbf{h}\cdot\kappa)\chi = 0, \tag{13}$$

where $\kappa = (\mathbf{b}\cdot\nabla)\mathbf{b}$ is the magnetic field line curvature, $\mathbf{b}$ is the unit vector along the field lines, χ is the eigenfunction, λ is the eigenvalue, $\mathbf{h} = \mathbf{B}\times\nabla S/B^2$ and $h^s = \mathbf{h}\cdot\nabla s$. Because the field lines in the Boozer magnetic coordinates are straight, we have $\nabla S = \nabla\phi - q(s)\nabla\theta - q'(s)(\theta-\theta_k)\nabla s$, where $q(s) = d\Phi/d\Psi$ is the inverse rotational transform. Furthermore, the simplified form of the magnetic field in the covariant representation in the magnetic coordinates allows us to demonstrate from the effective charge conservation relation $\nabla\cdot\mathbf{K} = 0$, after applying MHD force balance, that

$$(\sqrt{g}\mathbf{B}\cdot\nabla)\left(\frac{\mathbf{K}\cdot\mathbf{B}}{B^2}\right) = \frac{\tau}{\sigma+\tau}\left(\left.\frac{\partial p_\parallel}{\partial s}\right|_B + \frac{\sigma}{\tau}\left.\frac{\partial p_\perp}{\partial s}\right|_B\right)\left\{\frac{\partial}{\partial\theta}\left[\frac{I(s)}{\sigma B^2}\right] + \frac{\partial}{\partial\phi}\left[\frac{J(s)}{\sigma B^2}\right]\right\}. \tag{14}$$

This expression is proportional to the geodesic magnetic curvature contribution to the ballooning mode driving term. The ballooning mode equation becomes

$$\frac{\partial}{\partial\theta}\left\{\left[C_p + C_s(\theta-\theta_k) + C_q(\theta-\theta_k)^2\right]\frac{\partial\chi}{\partial\theta}\right\} + (1-\lambda)\left[d_p + d_s(\theta-\theta_k)\right]\chi = 0, \tag{15}$$

where $C_p = [\sigma g_{ss}/\sqrt{g} - (\sigma B_s)^2/(\sigma\sqrt{g}B^2)]$, $C_s = 2q'(s)\Psi'(s)A_4(s,\theta,\phi)/(\sigma\sqrt{g}B^2)$, $C_q = [q'(s)\Psi'(s)]^2\sigma^2|\nabla s|^2/(\sigma\sqrt{g}B^2)$, $\Psi'(s)d_s = -q'(s)(\sqrt{g}\mathbf{B}\cdot\nabla)(\mathbf{K}\cdot\mathbf{B}/B^2)$ and the nonsecular component of the driving term after invoking radial force balance is

$$d_p = \frac{1}{[\Psi'(s)]^2}\frac{\tau}{\sigma+\tau}\left(\left.\frac{\partial p_\parallel}{\partial s}\right|_B + \frac{\sigma}{\tau}\left.\frac{\partial p_\perp}{\partial s}\right|_B\right)\left[\frac{\sqrt{g}}{\tau B^2}\left.\frac{\partial p_\perp}{\partial s}\right|_B + \frac{[J(s)\Psi''(s) - I(s)\Phi''(s)]}{\sigma B^2} - \frac{\partial\sqrt{g}}{\partial s} + \sqrt{g}\mathbf{B}\cdot\nabla\left(\frac{B_s}{B^2}\right)\right]. \tag{16}$$

The asymptotic analysis of the ballooning mode equation yields the Mercier criterion. Because the geodesic magnetic curvature can be expressed in terms of the derivative along the field lines of the effective parallel current density function, a very useful closed form can be derived for the Mercier criterion in the Boozer coordinates which is not evident in other coordinate systems [15], namely

$$< h_q >< d_p > - < h_q >< d_q > + < h_q d_q > + < h_q >< h_q d_q^2 > - < h_q d_q >^2 \leq \frac{1}{4}, \tag{17}$$

for stability, where $d_q = -q'(s)(\mathbf{K}\cdot\mathbf{B}/B^2)$ and $h_q = 1/C_q$ and $< f >$ is the flux surface average of f. This criterion agrees with a form derived in Hamada coordinates [12].

4. Summary

Auxiliary heating methods and nonuniform losses of energetic particles can cause significant pressure anisotropies in magnetic confinement systems. We have formulated the global and local 3D linear MHD stability variationally in the limit of a fully interacting anisotropic pressure fluid from the universal term of the Kruskal-Oberman energy principle. We have adopted for this purpose the Boozer magnetic coordinate system, appropriately modified for anisotropic plasmas. The 3D MHD equilibrium state is constrained to have nested magnetic flux surfaces. The effective parallel current density is identified as an important source of free energy for MHD instabilities due to its singular nature on rational magnetic surfaces in 3D systems. The energy principle is Fourier decomposed in the periodic angular variables and finite elements are applied for the radial discretisation to reduce the global MHD stability problem to a special block pentadiagonal matrix eigenvalue equation that can be solved with an inverse vector iteration method. The local MHD stability is investigated through the formulation of the 3D ballooning equation in Boozer coordinates. In these coordinates, the geodesic magnetic curvature is demonstrated to be related to the effective parallel current density. This allows the asymptotic analysis of the ballooning equation to yield a closed form for the Mercier criterion.

References

[1] H. Yamada, K. Ida, H. Iguchi, S. Morita, O. Kaneko et al., Nucl. Fusion **32** (1992) 25.

[2] W. A. Cooper, S. P. Hirshman, S. Merazzi, R. Gruber, Comput. Phys. Commun. (1992) in press.

[3] S. P. Hirshman, O. Betancourt, J. Comput. Phys. **96** (1991) 99.

[4] K. A. Buckle, W. N. G. Hitchon, J. L. Shohet, Nucl. Fusion **25** (1985) 247.

[5] W. A. Cooper, Plasma Phys. Contr. Fusion **34** (1992) 1011.

[6] R. L. Miller, Phys. Fluids **29** (1986) 1176.

[7] M. N. Rosenbluth, S. T. Tsai, J. W. Van Dam, M. G. Enquist, Phys. Rev. Lett. **51** (1983) 1967.

[8] L. J. Zheng, S. T. Tsai, Phys. Fluids B **4** (1992) 1416.

[9] M. D. Kruskal, C. R. Oberman, Phys. Fluids **1** (1958) 275.

[10] A. H. Boozer, Phys. Fluids **23** (1980) 904.

[11] R. L. Dewar, A. H. Glasser, Phys. Fluids **26** (1983) 3038.

[12] J. L. Johnson, R. J. Hastie, Phys. Fluids **31** (1988) 1609.

[13] G. O. Spies, D. B. Nelson, Phys. Fluids **17** (1974) 1865.

[14] D. V. Anderson, W. A. Cooper, R. Gruber, S. Merazzi, U. Schwenn, Int. J. Supercomp. Appl. **4** (1990) 34.

[15] W. A. Cooper, Phys. Fluids **28** (1985) 754.

Nonlinear Response of the Tearing Mode to External Field Perturbations in a Flowing Plasma

R.D. Parker

Centre de Recherches en Physique des Plasmas
Association Euratom – Confédération Suisse
Ecole Polytechnique Fédérale de Lausanne
Av. des Bains – CH 1007 Lausanne, Switzerland

1. INTRODUCTION

It is well known that small field perturbations can induce or interact with magnetic islands in a tokamak to degrade confinement, in some cases to the point of disrupting the discharge e.g.[1-4]. The perturbations may arise intentionally through the application of helical current coils around the plasma or more seriously as a result of small errors in the position of field coils. Even though field errors are nearly always present there effect inside the plasma is often screened out by the intrinsic or induced rotation of the plasma. As a consequence magnetic islands are sometimes observed to be suppressed, or to rotate at small amplitude while at other times to slow down and lock at a particular toroidal angle leading to an increase in island width that can result in a disruption.

In an endeavour to understand the basic mechanisms behind these interactions a simple 2D slab model of reconnection on a current channel with an ExB drift to drive a flow and a corrugated conducting wall to generate a field perturbation was developed. The numerical model was first applied to the tearing stable case to investigate the flow suppression of error field induced magnetic islands[5,6].

In the present report the study is extended into the tearing unstable regime to explore the interaction of internally as well as externally driven reconnection processes in the presense of flow. Unlike the error field islands, the tearing mode islands are free to drift along with the plasma so that the flow suppression is to some degree replaced by a mechanism of mode-locking. As will become apparent from the simulations the interaction can be quite complex.

2. MODEL

The basic numerical model adopted is that of a 2-D, plane-slab plasma sandwiched between two perfectly conducting walls (at $x = \pm X_w$) with periodic boundary conditions in the y-direction (of periodicity length L_p). An approximately sinusoidal perturbation of the walls of amplitude δW ($\propto \delta B$) is introduced along the y-direction to provide a selfconsistant source of field error. Details of this can be found in ref.[5]. The initial equilibrium is $B = B_0 \tanh(x)$, It has a line of field reversal at x=0 along which reconnection can occur and is maintained by a y-directed electric field and a non-uniform resistivity profile. To produce the plasma flow an initially uniform ExB drift is driven in the y-direction by maintaining a potential difference between the walls.

To follow the evolution of the tearing mode in response to the error field, the visco-resistive MHD equations are integrated in time using a semi-implicit, spectral (in y)/ finite difference (in x) scheme. The stability of the tearing mode is controlled by adjusting the wall separation, X_w.

3. TEARING STABLE CASE

Before considering the effect of the tearing mode a simpler study[6] was first made of the effect of flow on magnetic islands induced by a stationary error field alone. The main result of this is that the error field magnetic islands can be suppressed by flow above a critical velocity: V_c. The island is initially able to grow to the width of the reconnection layer unobstructed since the field in this region is decoupled from the flow due to finite resistivity. However because of the flux freezing constraint the flow must be removed from the island before it can extend into the ideal region beyond the reconnection layer. Under the influence of the error field the flow is driven out of the island but if the limit on the maximum velocity shear does not allow it to vanish the island will remain suppressed. This predicts $V_c \propto \delta B\, S^{-2/5}\, \nu^{-2/3}$ [6] in good agreement with numerical results.

4. MARGINALLY UNSTABLE CASE

In general, instability to the tearing mode allows a rotating island to grow beyond the reconnection layer so that the suppression mechanism mentioned above nolonger occurs. The effect of the error field is then predominantly to stop the island rotating. However fig.1(b) shows that close to marginal stability the tearing mode can be made weak enough to still allow full suppression of the locked mode over a small range of velocities,

$V_c < V < V_L$, just below that for which it becomes unlocked. The transition to the suppressed state is discontinuous as a function of flow velocity and occurs at the same value V_c as for the marginally stable case of fig.1(a). However instead of becoming more and more suppressed as the flow is increased the island develops a steady state oscilation in position and amplitude. Just below V_L the island rocks back and forth between 50 and 160 degrees out of phase with the error field while the amplitude oscilates within the shaded region shown on the plot. In effect the tearing mode induces the island to grow but as it is dragged out of phase by the flow it is increasingly suppressed by the error field. The island then reduces in size until the magnetic torque of the error field causes it to flip back or reform closer in phase. Just above V_L the flow velocity is sufficiently high to drag the O-point of the island past the maxima in the error field so that the island begins to rotate.

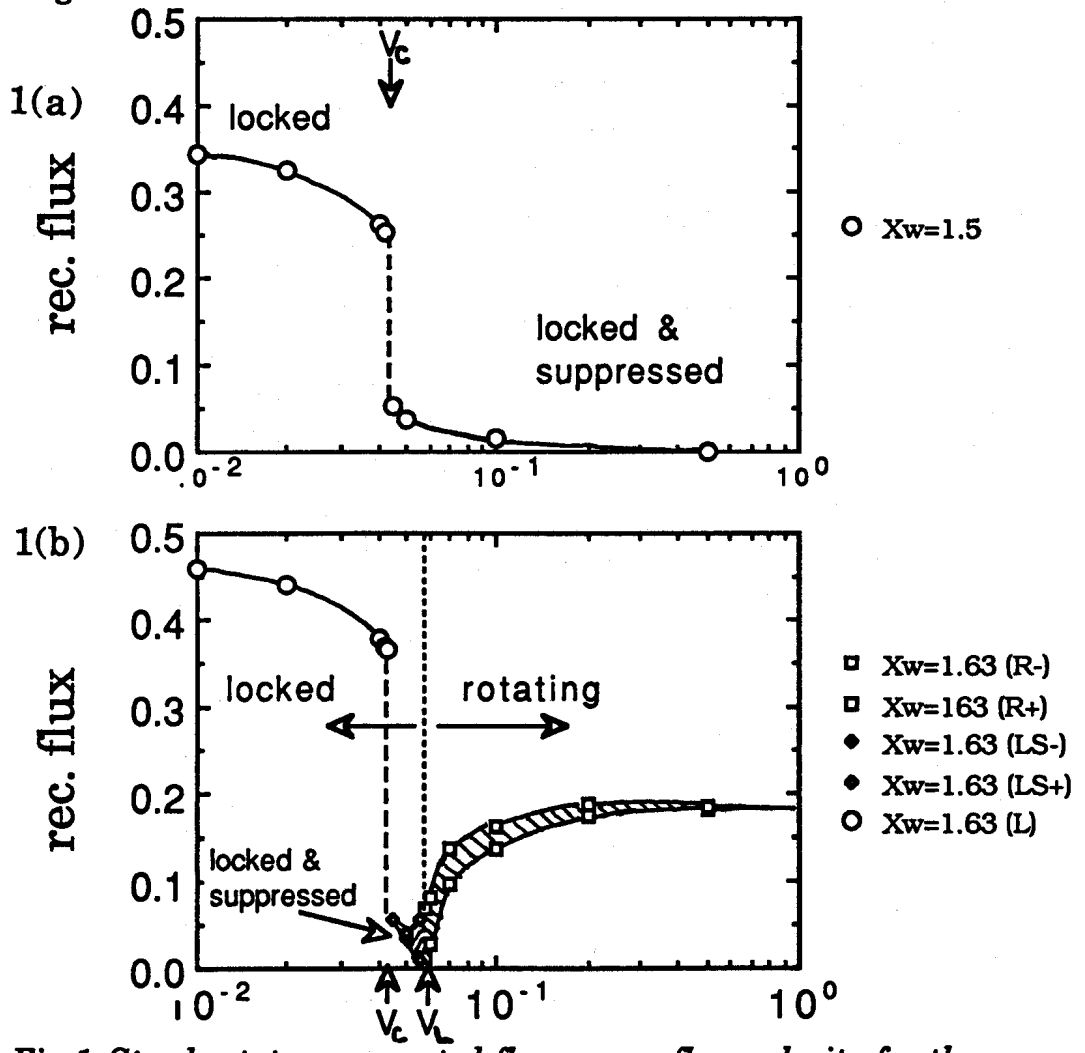

Fig.1 Steady state reconnected flux versus flow velocity for the (a) marginally stable (Xw=1.5) and (b) marginally unstable (Xw=1.6) cases, with $S=10^3$, $\nu=10^{-3}$, $Kp=0.35$, and $\delta W=0.02$.

The island still oscilates in amplitude as it moves in and out of phase with the error field. It also moves more slowly as the O-point approaches the maxima of the error field. This is where it is being suppressed so the net effect is to keep the amplitude small. As the flow is increased the island has less time to respond to the error field so that the amplitude of the oscilation decreases and the mean width of the island approaches the size it would have in the absense of the error field.

Well above marginal stability the full suppression of the locked mode nolonger occurs except when the amplitude of the error field is made very large as in fig.2 for the case with $\delta W = 0.08$. In this case the fully suppressed locked mode does not transform smoothly into the rotating mode as the velocity is increased. The rotating mode is also much larger and is actually stable for the same range of flow velocities.

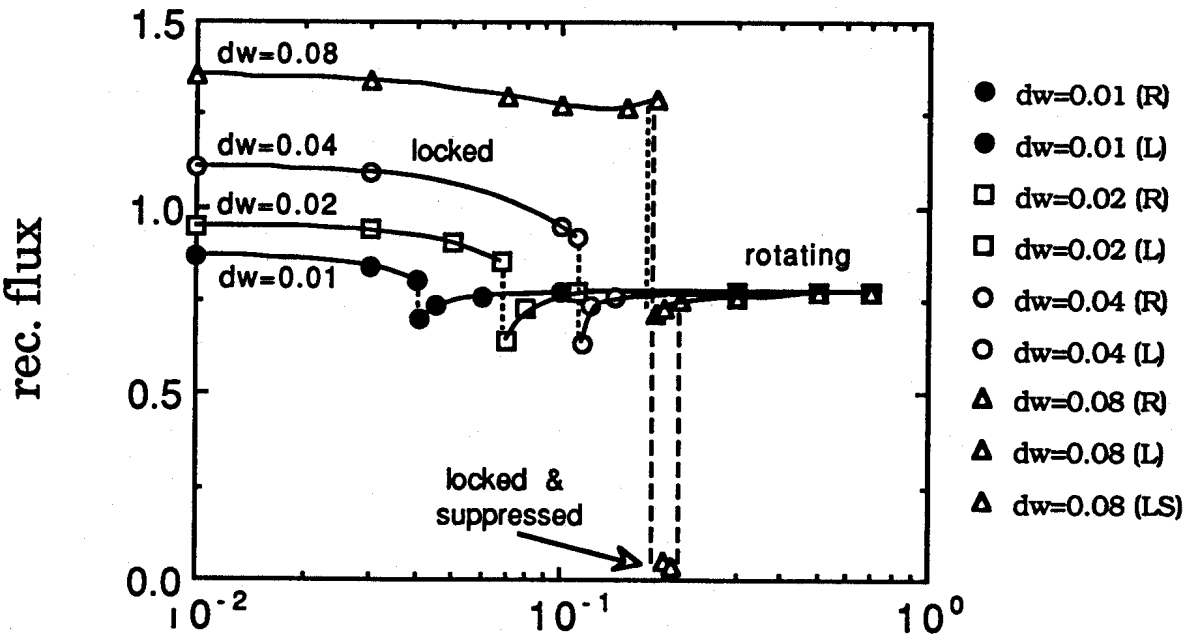

Fig.2 Steady state reconnected flux versus flow velocity for $\delta W = 0.01$, 0.02, 0.04, and 0.08 with $S=10^3$, $\nu=10^{-3}$, $X_w=2.$, $K_p=0.35$, $\delta W=0.02$

5. MODE LOCKING

Except when close to marginal stability, the tearing mode dominates the initial growth phase of the island so that inspite of the error field the island almost immediately starts to rotate.

The magnetic coupling to the error field, although weak to begin with, increases in strength as the island grows larger. If the island exceeds a critical width: W_L, the magnetic coupling dominates over the inertial and viscous forces to completely stop the rotation of the island.

Since the inertial and viscous torques increase with the flow locking occurs below a limiting velocity V_L. For $V << V_L$ the drag of the rotating plasma is so weak that the island does not need to grow very large to produce the magnetic coupling needed to lock the mode. In this case the island locks at a very early stage in the evolution. The closer V is to V_L the larger the

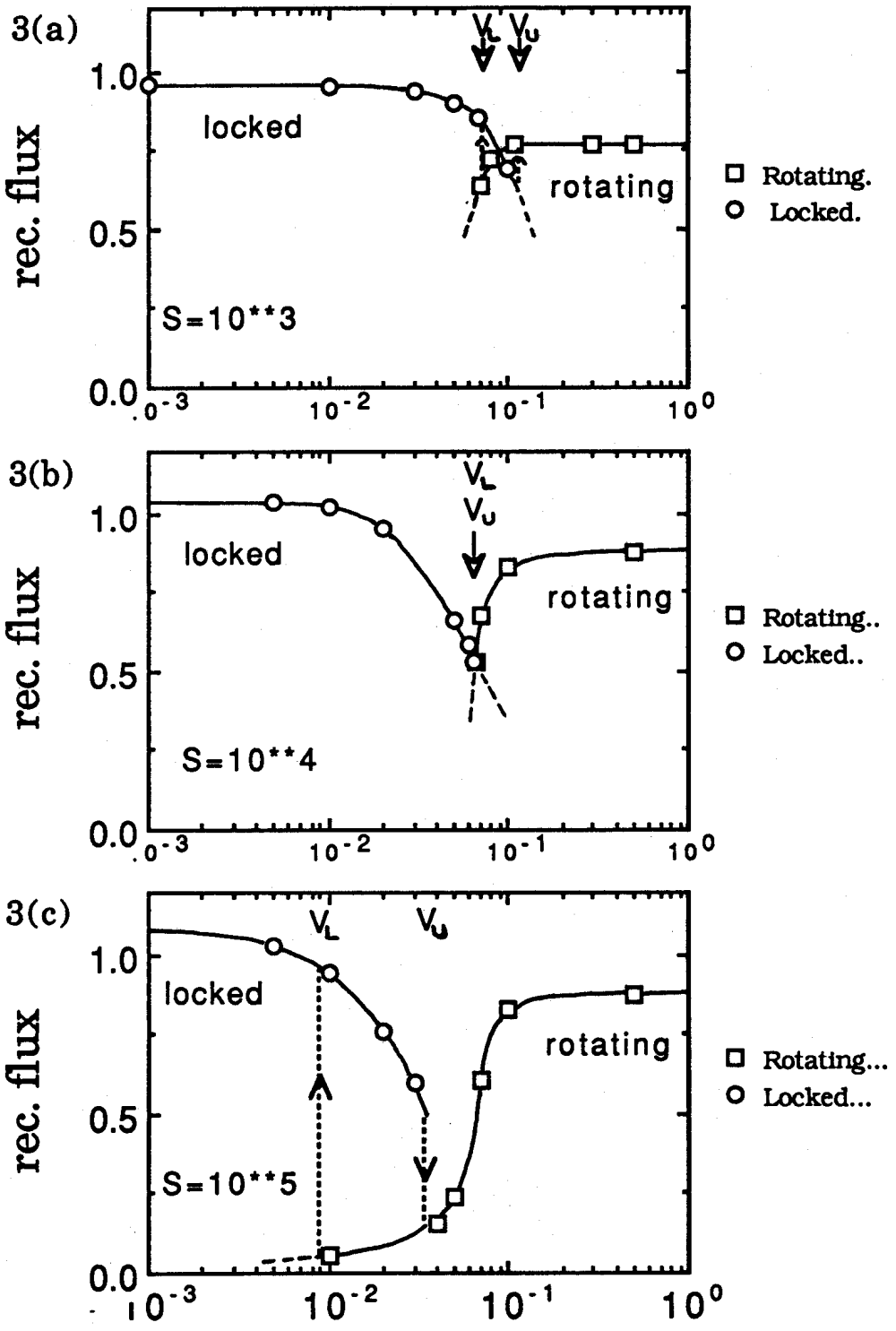

Fig.3 Steady state reconnected flux vs. flow velocity for (a) $S=10^3$, (b) $S=10^4$, and (c) $S=10^5$ with $\nu=10^{-3}$, $X_w=2.0$, $K_p=0.35$, $\delta W=0.02$

island grows before locking. For $V > V_L$ the island saturates at an amplitude too small for the magnetic coupling to overcome the drag of the surrounding plasma and so the island continues to rotate.

Raising the amplitude of the error field also strengthens the coupling between island and error field so that the same size tearing mode island can be induced to lock in a faster flowing plasma. In fact from fig.2 it can be seen that $V_L \propto \delta B$. An alternative way of viewing this is to say that locking occurs above a critical error field amplitude: δB_L, and that this limit is proportionately higher in a faster rotating plasma. Fig.4 shows that reducing the drag on the island by decreasing the viscosity allows it to lock at a higher flow velocity

6. MODE UNLOCKING

By restarting simulations with an already locked island state, computed from earlier runs with lower S,ν or V, the locked mode can be shown to unlock at a velocity V_U in general greater than the velocity V_L for which the rotating mode locks. That is, hysteresis occurs in the interval, $V_L < V < V_U$, within which the two attractors are locally stable.

To understand this we first note that the locked tearing mode is generally larger than the rotating mode due to the additional reconnection induced by the error field. It is consequently more strongly coupled to the error field so that either the error field amplitude must be reduced to decrease the magnetic coupling or the flow velocity raised to increase the drag on the island in order to unlock it.

This is partially compensated for by the fact that the locked mode becomes increasingly suppressed or attenuated as the flow is increased towards V_L. Figs.3(a) to (c) show that the onset velocity V_{LS} for suppression of the locked mode decreases steadily with resistivity and is probably why V_U also decreases with resistivity.

In the case of fig.3(a) the locked mode attractor close to V_U is stable for an island width smaller than that of the rotating mode attractor at the same velocity. The critical island width for unlocking therefore cannot be the same as for locking otherwise it would have unlocked.

7. ISLAND SUPPRESSION (and Enhancement)

Towards zero flow the amplitude of the locked mode, in terms of the reconnected flux, is simply the sum of the contributions due to the tearing mode and the error field. As the flow is increased around the locked island

the consequent increase in drag causes the island to be attenuated or partially suppressed above a velocity $V_{LS} < V_L$.

This is with the exception of the weak viscosity case shown in fig.4 in which the island is actually enhanced by the flow before locking. This enhancement effect was also found for the error field induced island of the tearing stable case[6] when $\nu << \eta$ and $V_c > 0.1V_A$ (V_A = Alfven velocity).

Toward large flow the amplitude of the rotating mode is just that due to the tearing mode alone as the effect of the error field is screened out by the flow. As the flow is reduced to where the rotating mode can start to respond to the error field it is increasingly suppressed via the mechanism described in section 4. The flow velocity V_{RS} below which this occurs appears to be almost independent of S, while the locking velocity V_L decreases with S so that for the $S=10^5$ case of fig. 3(c) the rotating island can be highly suppressed. At such small amplitudes the rotating island is found to transform into a rotating double island.

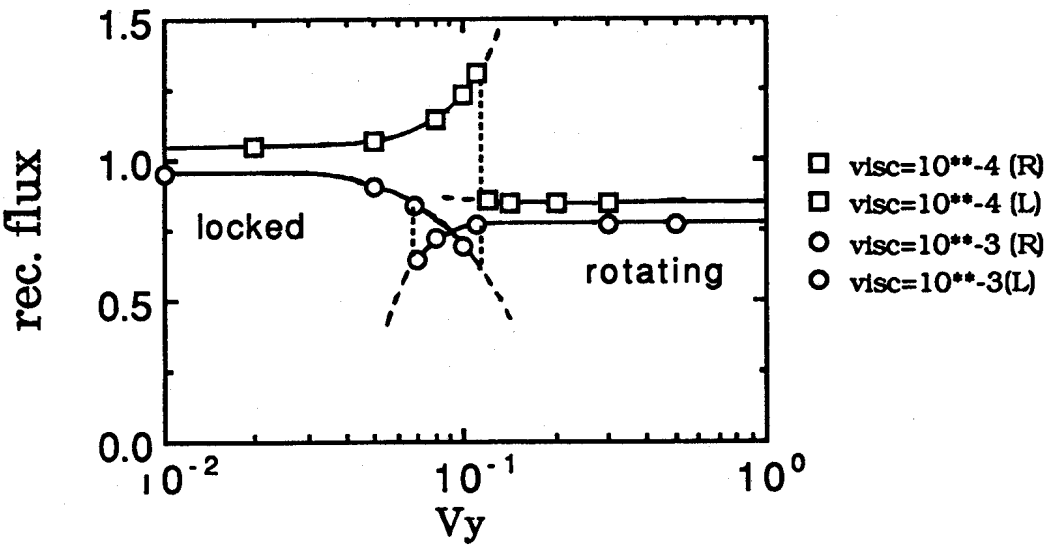

Fig.4 Steady state reconnected flux vs flow velocity for different viscosities: $\nu=10^{-3}$ and 10^{-4} with $S=10^3$, $X_w=2.$, $K_p=0.35$, $dW=0.02$

8. SUMMARY AND DISCUSSION

In summary the locked mode attractor is observed to show mode suppression roughly above some velocity V_{LS} and go unstable (unlock) above a the velocity V_U while the rotating mode attractor shows mode suppression roughly below the velocity V_{RS} and goes unstable (locks) below the velocity V_L.

The time evolution shows that rotating tearing mode magnetic islands lock in phase with an error field when the island width exceeds a

threshold width corresponding to when the magnetic coupling to the error field just dominates over the inertial and viscous forces.

Over the range of parameters tested so far: all four critical velocities increase roughly in proportion to δB; V_{LS}, V_L and V_U decrease with increasing S while V_{RS} is almost independent of S. This dependence on S leads to situations as in fig.3(c) where a highly suppressed rotating mode is simultaneously stable with a fully reconnected locked mode over a range of velocities. Such conditions would perhaps explain why, for example, the application of helical current coils around a tokamak can on some occasions suppress MHD activity while on others lead to disruption.

Reducing the viscosity can lead to enhancement instead of suppression of the locked mode as the flow is increased.

For the tearing stable case, islands induced by error fields can be highly suppressed above a critical velocity $V_c \propto \delta B\ S^{-2/5}\ \nu^{-2/3}$ [6]. This scaling is not predicted by a previous analytical treatment[7] due to the use of approximations not valid when the island is on the scale of the resistive layer width.

The simulations show that even for the tearing unstable case the islands and in particular the rotating mode (see fig.3(c)) can become highly suppressed. Since this brings the island close to the scale of the resistive layer it is also not clear that the the analytic treatment will be able to correctly predict the onsets for locking and unlocking.

Perhaps a manifestation of this problem is the fact that the analytic treatment predicts a limiting phase shift for the locked modes of $\pi/2$ whereas the simulations show that the o-point of a suppressed locked mode can be as much as π out of phase with the error field.

Acknowledgement: This work was partly supported by the Swiss National Science Foundation.

REFERENCES

[1] F. Karger et. al, Proc. 5th.IAEA conf., Tokyo, Vol.1, 207, (1974).

[2] P.R. Thomas et. al., Proc.10th IAEA conf., London, Vol.1, 353, (1984).

[3] A.W. Morris et al., Proc. 17th.EPS conf., Amsterdam, Vol.1, 379, (1990).

[4] J.T. Scoville et. al., Nucl. Fusion, 31, 875, (1991).

[5] R.D. Parker, R.L. Dewar, Comp. Phys. Com., 59, 1, (1990),

[6] R.D. Parker, Proc. 19th. EPS-ICPP conf., Innsbruck, Vol.1, 427, (1992).

[7] R. Fitzpatrick, T.C. Hender, Phys. Fluids B, 3, 644, (1991).

DAMPING OF GAP MODES: GEOMETRICAL AND PROFILE EFFECTS

L. Villard and G.Y. Fu*
Centre de Recherches en Physique des Plasmas
Association Euratom - Confédération Suisse
Ecole Polytechnique Fédérale de Lausanne
21, Av. des Bains, CH-1007 Lausanne, Switzerland
* Plasma Physics Laboratory, Princeton University, Princeton, USA

ABSTRACT - The damping of toroidicity and ellipticity induced Alfvén eigenmodes (TAE, EAE) in tokamak plasmas is studied for a wide variety of cases with the global wave finite element code LION.

1. Introduction

Any break of circular cylindrical symmetry removes the degeneracies of the cold plasma or ideal MHD continuous spectrum and creates gaps. In addition, a new class of Alfvén eigenmodes exists in these gaps. They have been named after the geometrical effect they stem from: Toroidicity induced (TAE) [1], Ellipticity induced (EAE) [2], etc., under the generic name of gap modes. The toroidicity induced gaps are created around $q = q_T = q_T = (|m| + 1/2)/|n|$, $\omega = \omega_T = 1/2q\sqrt{\rho}$, where m and n are the poloidal and toroidal wavenumbers, respectively, q is the safety factor and ρ is the mass density. The ellipticity induced gaps are created around $q = q_E = (|m|+1)/|n|$, $\omega = \omega_E = 1/q\sqrt{\rho}$. The number of gaps in the plasma is thus $|n|(q_a-q_o)$ where q_o and q_a are the values of q on axis and on boundary, respectively. Non-uniform profiles of $1/q\sqrt{\rho}$ imply that the gaps do not overlap and gap modes are continuum damped. Detailed studies of this effect can be found in Ref. [3]. A few examples will be shown in Section 4.

Besides continuum damping we examine other mechanisms that contribute to the stabilization of gap modes, in particular electron Landau damping. We also briefly mention how finite Larmor radius and

finite drift orbit size affects the α particle driven instability of gap modes. We are thus able to give a reasonable physical explanation of important aspects of the experimental results obtained so far in TFTR and DIII-D [4,5] and to expose important parameters that influence the stabilization of gap modes.

2. Continuum Damping and Kinetic Damping

We consider a plasma in axisymmetric ideal MHD equilibrium. The equilibrium is obtained from the Hermite bicubic finite element code CHEASE [6]. The plasma is surrounded by a pure vacuum region enclosed by a conducting wall. An antenna on which currents are prescribed with given toroidal wave number n and frequency ω is placed in the vacuum region. In the plasma we have

$$\nabla \times \nabla \times \vec{E} = \frac{\omega^2}{c^2} \vec{\vec{\varepsilon}} \bullet \vec{E} \qquad (1)$$

where $\vec{\vec{\varepsilon}}$ is the dielectric tensor operator. Detailed expressions of Eq. (1) in toroidal geometry can be found in Ref. [7]. We consider first the cold, current carrying, plasma model with zero electron inertia. [For $\omega/\omega_{ci} << 1$ it is identical to ideal MHD with $\gamma_p = 0$.] Equation [1] is singular at the spatial Alfvén resonances occurring on magnetic surfaces (ψ = const.) satisfying $(\varepsilon_{\psi\psi} - K)E_\psi = 0$, where K is a differential operator involving $\vec{B} \bullet \nabla$ [8]. The singularities are resolved in a similar way to the Landau damping problem. An imaginary part is added to $\varepsilon_{\psi\psi}$: ω is replaced by $\omega(1+i\nu)$, with $\nu > 0$ to ensure causality. The operator (1) is now regularized. Its eigenfunctions and eigenfrequencies are complex. Equation 1 is discretized using a non-conforming, non-polluting finite element scheme implemented in the LION code [7]. The limit $\nu \to 0$ is obtained numerically. It yields finite damping, therefore ν should not be mistaken for the damping rate. The total absorbed power vs applied frequency, $P(\omega)$, is calculated. When a global mode is excited it shows as a peak on $P(\omega)$. The position of the peak gives the real part of the eigenfrequency, $Re(\omega_o)$, and the half width at half maximum (HWHM) gives the damping $\gamma = Im(\omega_o)$. Note that the solution for $\nu \to 0$ differs from the solution for $\nu = 0$: the non-analytical behaviour of the eigenfunction around the resonances prevents from making an

expansion in ν. With finite ν there is formally speaking no more continuum but a discrete set of damped complex eigenmodes. We shall nevertheless use the terminology "continuum damping" for the cases where $\mathrm{Re}(\omega_o)$ lies within the continuum frequencies formally defined for $\nu = 0$, although the proper term is "resonance absorption damping".

The inclusion of kinetic effects (FLR) and finite m_e modify the spectrum. The continuum is replaced by a discrete set of damped eigenmodes of the kinetic Alfvén wave (KAW) and surface quasi-electrostatic wave (SQEW). Resonance absorption is replaced by mode conversion to either a KAW (if $v_{te} > v_A$) or a SQEW (if $v_{te} < v_A$). The total power absorption is the same as the cold plasma theory prediction, unless the KAW or SQEW is undamped before reaching the plasma centre or edge: resonance absorption does not depend on the detailed dissipation mechanism. If the global mode has no resonance surface and if the damping rate is small, kinetic effects can be treated perurbatively. Let $\vec{\vec{\varepsilon}}^{(k)}$ be the dissipative part of the hot plasma dielectric tensor operator and let us apply it to the cold plasma eigenfunction $\vec{E}$. For example, the global collisionless electron Landau damping of Alfvén modes can be written as [3,8]

$$\left(\frac{\gamma}{\omega}\right)_L = \frac{\frac{\sqrt{\pi}}{2}\int \rho\, \hat{\rho}_i^2\, (v_A/v_{te})\, \exp(-v_A^2/v_{te}^2)\, |\nabla_\Lambda E_\psi|^2\, dV}{\frac{1}{2}\int \rho\, |\vec{E}|^2\, dV} \qquad (2)$$

where $\hat{\rho}_i$ is the ion Larmor radius with electron temperature, the integrals are on the plasma volume, and the subscript Λ denotes projection onto the plane $\perp \vec{B}_o$. Note that in a torus $k_\parallel$ is a differential operator. For TAE and EAE modes we find that $k_\parallel E_\psi \sim (\omega/v_A)E_\psi$. Treating kinetic effects perturbatively implies that we assume they introduce dissipation but do not affect the dispersive properties of the wave, which is clearly not true near the spatial Alfvén resonances.

Other damping mechanisms that may be important include the following. (1) Ion Landau damping is an order of magnitude smaller than electron Landau damping for TFTR and DIII-D experiments [4,5], but in a reactor one could have v_A/v_{ti} as small as 2. (2) Curvature drift collisionless electron Landau damping is $(\gamma/\omega) \sim q^2\beta_e v_A/v_{te}$. (3) Collisionality

of trapped electrons can give a substantial contribution to the damping. It was shown in Ref. [9] that it is proportional to

$$\left(\frac{\gamma}{\omega}\right)_{\text{col.trap.}} \propto (k_\perp \hat{\rho}_i)^2 \left(\frac{\bar{\nu}}{\omega}\right)^{1/2} \left\{ \ell n \left[16 \left(\frac{a/R}{\bar{\nu}/\omega} \right)^{1/2} \right] \right\}^{-3/2} \qquad (3)$$

where $\bar{\nu} = 4\pi n_e e^4 \ell n\Lambda / m_e^2 v_{te}^3$.

We point out that all these kinetic dampings, except (2) above which is one order of magnitude smaller than the others, increase quadratically with the toroidal mode number n. On the other hand, the growth rate of α particle driven instability was calculated in Ref. [9] with FLR and orbit size effects to increase linearly with the mode number up to a maximum when $k_\perp \rho_\alpha \simeq 1$ and to decrease asymptotically as $1/k_\perp\rho_\alpha$ for $k_\perp\rho_\alpha >> 1$. [Note that $k_\perp$ is proportional to m which is proportional to n.] Balance of these competing effects imply that intermediate n gap modes are the most unstable, which is in good agreement with experimental results so far [4,5].

3. A Semi-Empirical Formula for Electron Landau Damping

An example of TAE mode is shown in Fig. 1. The parameters are: $R/a = 3.2$, $\rho(s) = (1-0.99\ s^2)^{0.7}$, $n = 3$, $q_o = 1.05$, $q_a = 2.89$, $\beta = 0$. The wavefield extends over the whole plasma cross section and peaks around all gap positions where $q = (|m| + 1/2)/|n|$. The radial wavenumber is much larger than the poloidal wavenumber and is proportional to the local shear. This suggested us to propose a semi-empirical formula for the collisionless electron Landau damping. In circular plasmas with $R/a = 3.2$, parabolic T_e profiles and monotonic, quasi-parabolic q profiles, we found that $(\gamma/\omega)_L$ follows approximately:

$$\left(\frac{\gamma}{\omega}\right)_{L,FIT} \simeq 2.0 \times 10^{-4}\ n^2 (q_a - q_o)^2\ a^{-2}\ T_{eo}^{1/2}\ B_o^{-1}\ n_{eo}^{-1/2}\ A^{1/2} \qquad (4)$$

where a[m], B_o[T], $n_{eo}[10^{19}m^{-3}]$, T_{eo}[keV], and A is the ion mass in units of proton mass. Figure 2 shows $(\gamma/\omega)_L$ as calculated with the LION code vs $(\gamma/\omega)_{L,FIT}$ for a wide range of parameters: $n = 1\text{-}4$, $q_a = 2.5\text{-}5.0$,

a = 0.18-3m, T_{eo} = 1-40 keV, n_{eo} = 3-20 × $10^{19}m^{-3}$, B_o = 1-5T, A = 1-3. Good agreement is obtained over two orders of magnitude.

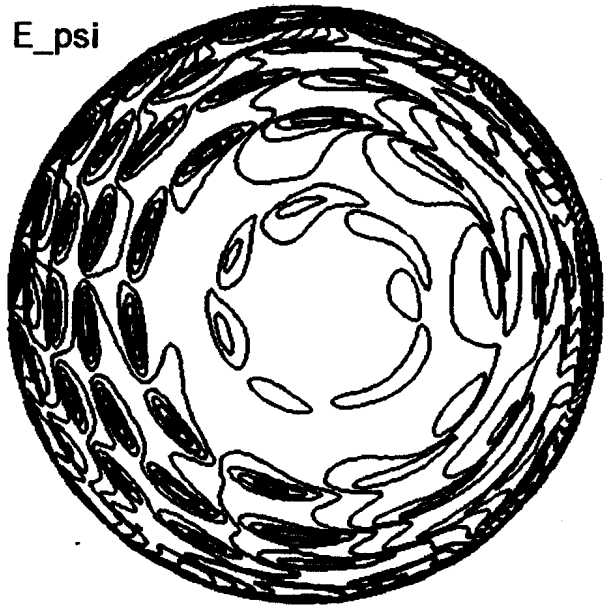

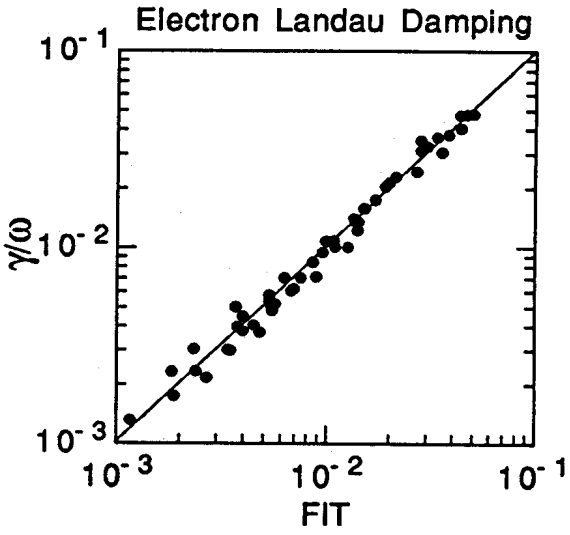

FIG. 1: *Contour plot of a n = 3 TAE electric field component Re(E_ψ). R/a = 3.2, $\rho = (1-0.99s^2)^{0.7}$, q_o = 1.05, q_a = 2.89, β = 0.*

FIG. 2: *Collisionless electron Landau damping rate of TAE modes vs semi-empirical formula, Eq. (4), in circular plasmas with R/a = 3.2 and parabolic T_e profiles.*

The numerical coefficient in Eq. (4) depends on aspect ratio, elongation and triangularity through the dependence of the eigenmode structure on these parameters. Unfortunately, in elongated and triangular plasmas, TAE and EAE modes are particularly peaked near the edge [3] where $v_A \simeq v_{te}$ and thus $(\gamma/\omega)_L$ strongly depends on details of the T_e profile and mode structure there. There is no simple scaling law with elongation or triangularity. Near the edge other physical mechanisms should be considered, in particular collisonal damping, especially if density is not too small and temperature is low.

4. Continuum Damping: Geometrical and Profile Effects

Figure 3 shows the continuum damping rate of the most weakly damped n = 2 and n = 3 TAE modes for various density profiles. The other parameters are: R/a = 3.2, circular, q_o = 1.05, q_a = 2.89, β = 0. Peaked ρ profiles with flat edge gradients (α = 0) or slightly hollow ρ profiles with steep edge gradients (α = 8) are such that $1/q\sqrt{\rho}$ is non uniform. Therefore, the gaps do not overlap and we have $(\gamma/\omega)_{cont}$ of the order of several percent. Note that for all cases considered here $(\gamma/\omega)_{cont} \tilde{>} 10^{-2}$. As a matter of fact, the gaps never overlap exactly and all gap modes found here have resonance surfaces.

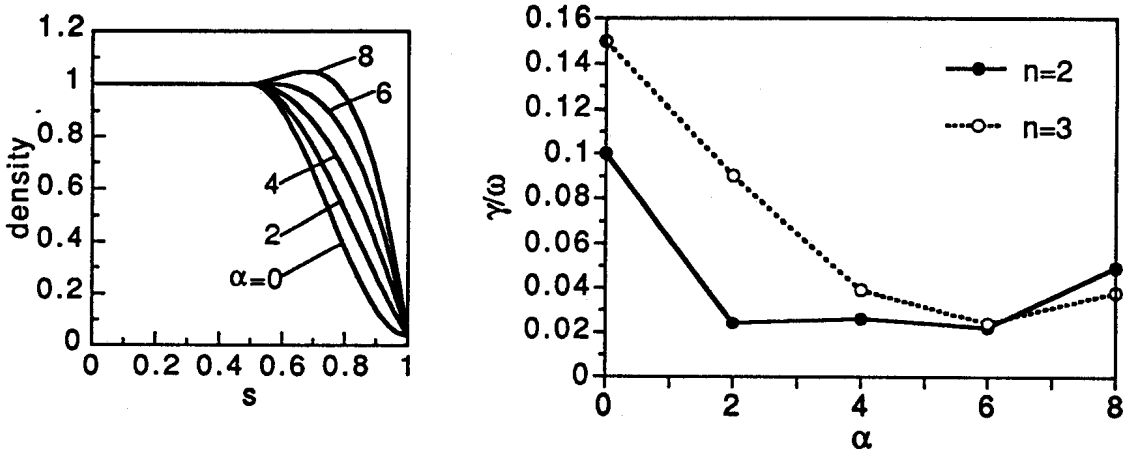

FIG. 3: *Continuum damping rate of the most weakly damped n = 2 and n = 3 TAE modes (right) for various density profiles (left). R/a = 3.2, q_o = 1.05, q_a = 2.89.*

We have also shown [3] that finite β_{pol} decreases frequencies of the gap modes. Even when the gaps overlap, the gap modes reach the lower gap edge and are continuum damped for β values below Troyon's limit. For example, for R/a = 3.2, q_o = 1.05, q_a = 2.89, we found the n = 1 TAE frequency to be

$$R_e(\omega_o) \tilde{=} 0.44\ (1\text{-}0.5\ \beta_{pol}) \qquad (5)$$

The effects of elongation (κ) and triangularity (δ), combined with finite aspect ratio, were studied in several sequences of equilibria. The most interesting result is shown in Fig. 4. It shows $(\gamma/\omega)_{cont}$ of the n = 1 EAE mode vs a/R for $\delta = 0$ and $\delta = 0.3$, in a plasma of elongation 2. For $\delta = 0$, $(\gamma/\omega)_{cont}$ is roughly proportional to $(a/R)^2$ owing to the toroidal coupling of the dominantly m = -3 wavefield near the elliptical gap $q_E = 2$ to a m = 0 resonance surface. For a given a/R, $(\gamma/\omega)_{cont}$ increases with δ, consistently with the triangularity coupling of m and m $\pm$ 3. For $\delta = 0.3$, $(\gamma/\omega)_{cont}$ decreases with a/R owing to the increase in the distance between the $q_E = 2$ elliptical gap and the m = 0 resonance surface. On the other hand, the TAE mode has $(\gamma/\omega)_{cont} = 0$ for all cases considered here. We conclude that triangularity can stabilize the EAE but not the TAE. This might be the reason why no EAE were observed in DIII-D [5].

The stabilization of TAE modes by continuum damping thus cannot be achieved by shaping the plasma cross section, but rather by $1/q\sqrt{\rho}$ profile effects. For ITER-like parameters (R/a = 2.8, $\kappa = 2$, $\delta = 0.4$), assuming a flat ρ profile, $q_o = 1.05$ and $q_a = 4.2$, we have found that $(\gamma/\omega)_{cont} > 5 \times 10^{-2}$ for all n = 1 and n = 2 TAE and EAE modes.

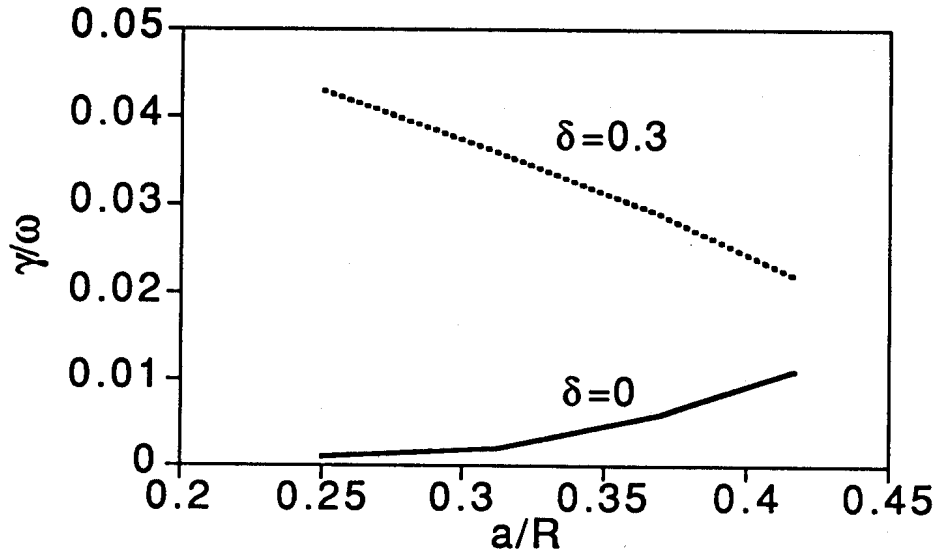

FIG. 4: *Continuum damping rates of n = 1 EAE modes vs inverse aspect ratio in plasmas with elongation $\kappa = 2$, triangularity $\delta = 0$ (continuous line) and $\delta = 0.3$ (dotted line).*

5. Conclusions

(1) TAE/EAE modes can be excited by an antenna placed in the vacuum region surrounding the plasma. (2) Electron Landau damping is proportional to n^2 and, therefore, may be the mechanism setting an upper limit on the n's that can go unstable. Other important kinetic damping mechanisms, such as collisionality of trapped electrons, also increase quadratically with n. (3) Gap modes can be continuum stabilized by finite pressure. (4) Triangularity can stabilize EAE modes. (5) Gap modes are continuum stabilized by non-uniform profiles of $1/q\sqrt{\rho}$. For ITER parameters, assuming flat ρ profiles, the continuum damping rate of all low n TAE and EAE modes is larger than 5×10^{-2}.

Acknowledgements: We would like to thank Dr. J. Vaclavik for many fruitful discussions and H. Lütjens for providing the equilibrium code CHEASE. This work was partly supported by the Swiss National Science Foundation.

References

[1] C.Z. Cheng, M.S. Chance, Phys. Fluids **29** (1986) 3695.

[2] R. Betti, J.P. Freidberg, Phys. Fluids B**3** (1991) 1865.

[3] L. Villard, G.Y. Fu, "Geometrical and profile effects on toroidicity and ellipticity induced Alfvén eigenmodes", Lausanne Rep. LRP454/92 (1992), accepted for publication in Nucl. Fusion (1992).

[4] K.L. Wong, R.J. Fonck, S.F. Paul et al., Phys. Rev. Lett. **66** (1991) 1874.

[5] W.W. Heidbrink, E.J. Strait, E. Doyle, G. Sager, R.T. Snider, Nucl. Fusion **31** (1991) 1635.

[6] H. Lütjens, A. Bondeson, A. Roy, Comput. Phys. Commun. **69** (1992) 287.

[7] L. Villard, K. Appert, R. Gruber, J. Vaclavik, Comput. Phys. Rep. **4** (1986) 95.

[8] J. Vaclavik, K. Appert, Nucl. Fusion **31** (1991) 1945.

[9] G.Y. Fu, C.Z. Cheng, "Excitation of high-n toroidicity-induced shear Alfvén eigenmodes by energetic particles and fusion alpha particles in tokamaks", submitted to Phys. Fluids B (1992).